Pergamon

0967-0637(95)00034-8

Deep-Sea Research I, Vol. 42, No. 8, pp. 1313–1357, 1995

0967-0637/95 $9.50 + 0.00

Coupled physical and biological modeling of the spring bloom in the North Atlantic (I): model formulation and one dimensional bloom processes

D. J. McGILLICUDDY Jr,* J. J. McCARTHY*
and A. R. ROBINSON*

(*Received* 31 *March* 1994; *in revised form* 9 *September* 1994; *accepted* 12 *January* 1995)

Abstract—This is the first of two papers that introduce a mesoscale eddy resolving coupled physical and biological model system. The physical model consists of a quasigeostrophic interior with a fully coupled surface boundary layer. The nitrogen based biological model includes nitrate, phytoplankton, heterotroph and ammonium fields. This interdisciplinary model system is used to examine aspects of the 1989 JGOFS North Atlantic Bloom Experiment data set. This paper deals mainly with one dimensional processes and a companion paper addresses three dimensional phenomena. The data set consists of two time series of observations taken from different water masses in the mesoscale environment. The general features of the two time series are well represented by a one dimensional model when the mesoscale *spatial* variability in the initial condition is treated explicitly within the one dimensional framework. However, a significant bias is evident in the first time series as the sampling pattern began in a warm feature and moved toward colder ones. Mistaking spatial for temporal variability in this case results in an apparent sink of heat and source of nitrate in the data. Removing this bias with the one dimensional model results in an *f*-ratio that is almost a factor of two higher (0.64) than computed by other authors based on nutrient inventories and primary productivity measurements (0.37). The second time series was conducted in the interior of a mesoscale feature and spatial biasing is minimal. The model forms a seasonal thermocline and nitracline that compare quite well with the data in both magnitude and vertical extent. A subsurface ammonium maximum is generated by the model from an initially homogeneous profile that also agrees well with the data. Simulated primary productivity profiles match ^{14}C incubations except on the final day of the simulation when surface nutrients appear in to have been exhausted slightly prematurely. Computed *f*-ratios are consistent with independent estimates based on uptake measurements. A systematic parameter dependence and sensitivity analysis is carried out on these results. The most sensitive parameters are the phytoplankton and heterotroph maximum growth rates. Detailed analysis of the behavior of the system indicates tight coupling between phytoplankton production and heterotrophic consumption even in the early stages of the bloom.

1. INTRODUCTION

This is the first of two papers in which a mesoscale eddy resolving coupled physical and biological model system is introduced and applied in the context of the 1989 JGOFS North

*Department of Earth and Planetary Sciences, Harvard University, Cambridge, MA 02138, U.S.A.; present address: Woods Hole Oceanographic Institution, Woods Hole, MA 02543, U.S.A.

Atlantic Bloom Experiment (NABE). In Part 1 the model system is formulated and a one dimensional implementation is used to examine aspects of the bloom that are primarily controlled by local forcing. The model then having been tuned to the NABE data in one dimension, the influence of mesoscale dynamical processes is investigated in Part II (McGillicuddy *et al.*, 1995) (hereafter MRM95).

The annual spring bloom in the Northeast Atlantic Ocean is an important event in terms of high trophic level dynamics and the carbon cycle. During the winter a combination of strong wind forcing and heat loss through the surface results in very deep mixed layers with high nutrient concentrations. Rates of primary productivity are generally low because the integrated light exposure of the phytoplankton is reduced when they are mixed over a large depth interval. When springtime stratification of the upper ocean shoals the mixed layer, integrated production exceeds losses due to respiration, sinking and grazing thereby causing a phytoplankton bloom (Riley, 1942; Sverdrup, 1953). This is a purely one dimensional process in which the relationship between the depth of mixing and the e-folding scale of the ambient light field determines the rate of primary production.

This classical one dimensional paradigm is quite useful in explaining the "early bloom" condition when phytoplankton populations are exclusively light limited. However, nutrient limitation plays an important role in the "late bloom" as surface nutrient concentrations become depleted. Under these circumstances three dimensional effects can be of primary importance. For example, the perturbation of the density field by mesoscale eddies produces significant spatial structure in the nutrient concentrations of the upper thermocline. This structure is projected to the surface by the deep mixing that sets the initial conditions for the bloom. That is, the late winter distribution of nutrients in the surface ocean contains a strong mesoscale signal. This mesoscale signal is superimposed on the large scale meridional gradient in wintertime surface nutrient concentrations that results from the north south variation in mixed layer depth (Glover and Brewer, 1988). As "early bloom" light limitation gives way to "late bloom" nutrient limitation, the spatial structure of the initial nutrient distribution results in corresponding biomass patterns. In this regard, mesoscale perturbations of the initial nutrient field allow the bloom to proceed farther in areas of enhancement, while reducing the magnitude of the biomass maximum in areas of depression.

Another fundamental three dimensional effect arises from the dynamics of mesoscale flows. The evolution of these features can cause intense vertical motions that transport nutrients toward the surface (Woods, 1988). Such transports can in fact further modify the initial nutrient distribution in the "early bloom" situation. However, their most important ramifications unfold in the later bloom stages. Mesoscale upwellings can serve to resupply phytoplankton growth in the "late bloom" period, and could represent the most important source of new nutrients in the oligotrophic "post-bloom" situation (MRM95).

Horizontal advection can also significantly influence biological and chemical distributions. Mesoscale flows can transport material over considerable distances, creating complex and convoluted structures. In contrast to the above dynamical processes which affect the *in situ* growth rate, advective processes generate variability simply by rearranging the fluid.

In addition to these three dimensional effects, there are a variety of essentially local processes that influence the evolution of the upper ocean. Surface fluxes of heat, fresh water and momentum cause variations in the mixed layer depth with corresponding entrainment and detrainment of nutrients and other important biological material.

Excursions of the mixed layer can create complicated remnant layer structures that are further modified by diffusion.

Physical, biological and chemical variability results from a combination of these effects and their interaction. Here a general interdisciplinary model system is introduced to examine these processes in detail. It is used in the context of the 1989 JGOFS NABE at 47°N, for which physical, biological and chemical data are concurrently available (see Ducklow and Harris, 1993, and references therein). The approach will be to first focus on one dimensional processes. Marra and Ho (1993) have modeled some aspects of the one dimensional bloom processes during the first of the two main observational periods during the experiment. Because a different water mass was sampled during the second observational period the two data sets cannot be reconciled in a single simulation with a one dimensional model. Here an attempt will be made to model the combined data sets with two parallel simulations using a one dimensional model in the absence of any eddy effects except for the spatially varying initial nutrient distribution.

2. EXPERIMENTAL DESIGN

In 1989 the JGOFS program staged a coordinated multinational effort to investigate the spring phytoplankton bloom in the North Atlantic along longitude 20°W from 15 to 60°N. One of the most intensively sampled locations was the 47°N site, which was occupied from late April to mid June with additional stations in July and August. During this time, altimetric data from Geosat and some *in situ* hydrographic measurements were used to define the mesoscale flow field in the vicinity of the experiment (Robinson *et al.*, 1993). Three cyclonic eddies ("Big," "Standard," and "Small") were observed to evolve and interact over the 10 weeks of observations (Fig. 1). Significant submesoscale variability was also documented.

Interpretation of the time series of biological observations is made difficult by the presence of mesoscale heterogeneity for a number of reasons. The issue of nutrient supply through mesoscale dynamical processes is a complex one and will be dealt with in MRM95. Here the effects of the mesoscale variability in the initial nutrient distribution will be addressed. These effects would not pose a problem to the interpretation of the time series if a single water mass were followed and sampled throughout the experiment. Unfortunately, such was not the case.

The time series of measurements can be conveniently split into two periods. Early in the time series (days 115–128) an area to the west of the Small eddy was sampled (Fig. 2a). The time series begins in the northern section of the submesoscale anticyclone to the west of the Small eddy and proceeds southward. On two occasions (days 117–118 and day 119) during this southward progression the stations are located far enough east that the frontal region between the anticyclone and the Small eddy is sampled. The ship then moved westward into a submesoscale cyclonic feature to the west of the anticyclone. After a cluster of measurements were made in this feature between days 122 and 125, the ship moved approximately 85 km eastward back to the frontal region between the anticyclone and the Small eddy. From this it can be argued that the time series is biased toward colder, more nutrient rich water masses. That is, the time series begins in the western anticyclone and then moves into colder features (the western cyclone and subsequently the Small eddy). This bias must be accounted for in interpretation of the data. Late in the time series (days 142–151) a group of stations were occupied in the interior of the Small eddy (Fig. 2b).

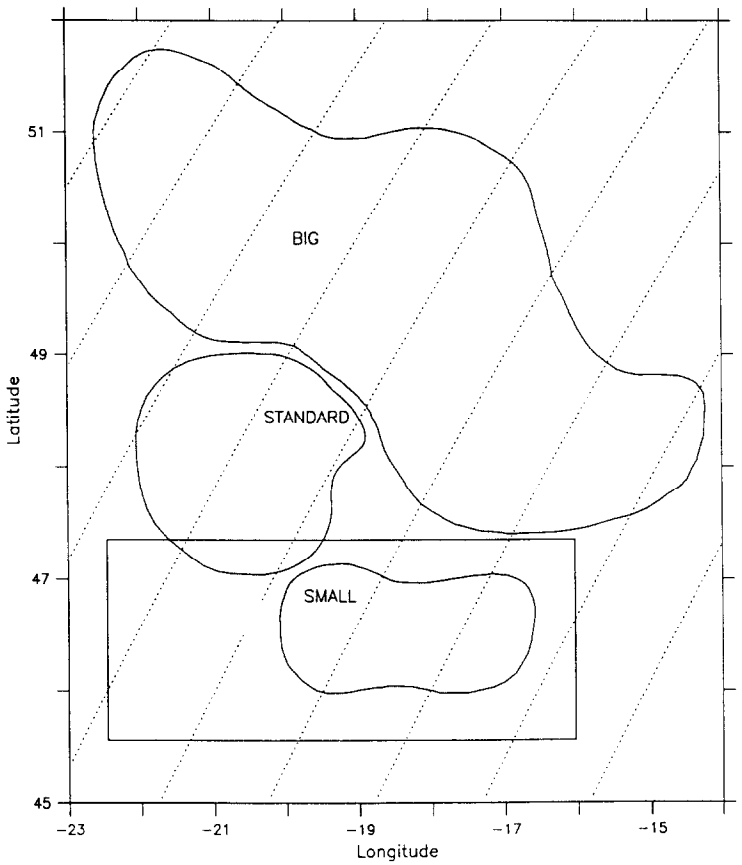

Fig. 1. Mesoscale eddy analysis for the period 8–24 May 1989 from Robinson *et al.* (1993). The three eddy features "Big", "Standard" and "Small" were identified from a combination of Geosat altimetric data (ground tracks shown as dotted lines) and hydrographic measurements. The rectangular box indicates the domain of the objective analysis shown in Fig. 2.

These observations were made in a small area of weak spatial gradients in the hydrographic field, so little bias in these measurements is expected.

These two time series (Early/Outside and Late/Inside) will be examined with a one dimensional coupled physical–biological model of the upper ocean. Because the two data sets come from different water masses, a single one dimensional simulation clearly cannot represent them both. Therefore two separate simulations ("Inside" and "Outside") are

Fig. 2. Objectively analyzed dynamic height at 25 m relative to 490 m for the first (a) and second (b) data periods in the rectangular domain shown in Fig. 1. The fields have been masked where expected error exceeds 50%. The letters indicate locations of the western flank of the Small eddy (A), the interior of the Small eddy (B), the western anticyclone (C) and the western cyclone (D). Physical and biological time series measurements are shown as open circles connected by a solid line. Locations of additional hydrographic observations are indicated by plus signs. The ship's location from year day 115 to 128 is indicated in (a). In (b) the time series spans days 142 through 151 as the ship moves first southward and then northeastward. Year days are indicated at the endpoints of the sampling period.

(a)

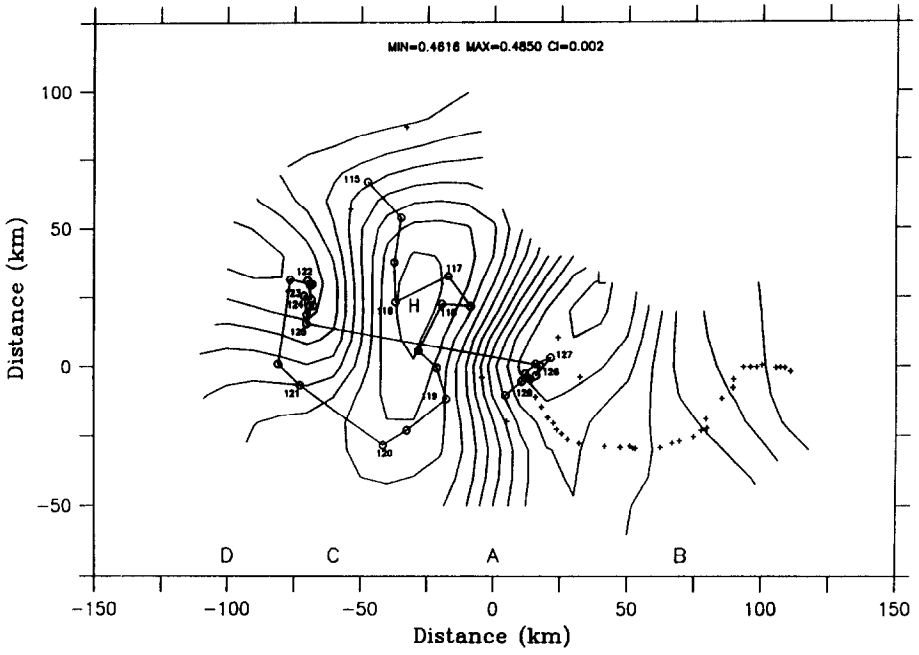

Dynamic Height at 25m: Early Period

(b)

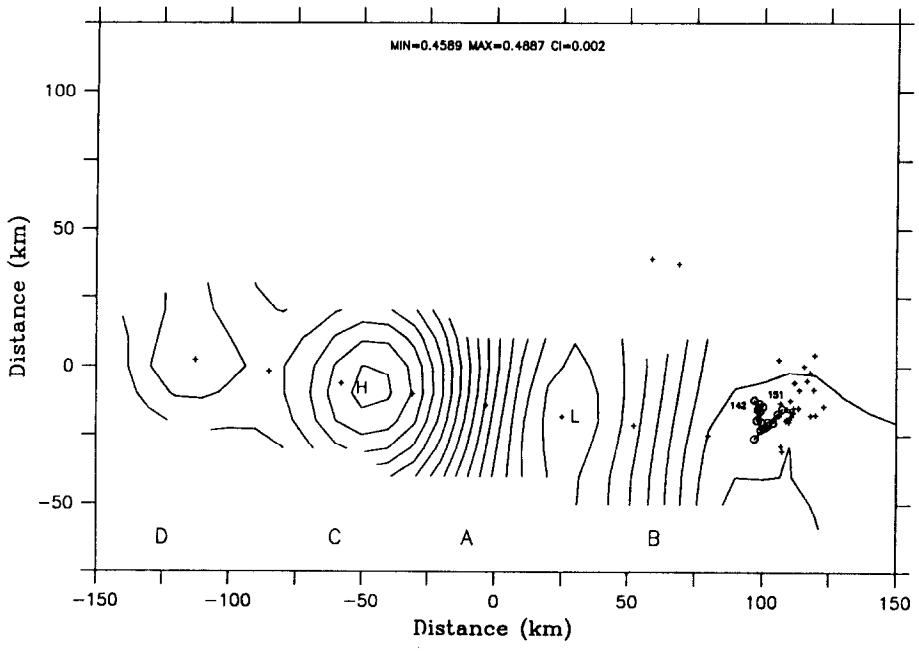

Dynamic Height at 25m: Late Period

carried out independently to reflect the different environments. Anticipating the initialization requirements of three dimensional modeling (MRM95 initialize on day 115 with full three dimensional fields), both simulations are initialized at the beginning of the experiment on day 115. It can be argued that this is not appropriate for modeling the Late/Inside data set because no data exist inside the eddy early in the experiment. However, a reasonable method for estimating the mesoscale perturbation in the pre-bloom nitrate distribution will be used to initialize the Late/Inside simulation on day 115. Concentrations of phytoplankton, heterotrophs and ammonium are assumed to be uniform and low in the late winter condition. Regardless of the initialization technique used in the Late/Inside simulation, the relevant point is that the model should run through the data where the data are available. The following simulations will show that two one dimensional simulations that differ only in their initial nitrate distribution can capture the main features of the observations.

3. METHODS

The various data sets used in this work were provided through the U.S. JGOFS database (Slagle and Heimerdinger, 1991). Hydrographic and nutrient data were collected by the Oceanographic Data Facility of the Scripps Institution of Oceanography. A Neil Brown CTD was used to collect conductivity and temperature profiles. A rosette of Niskin bottles was used to collect water samples for which nitrate, silicate and phosphate were measured with an autoanalyzer. High resolution nitrate and ammonium data were provided with pump profiles (Garside and Garside, 1993). Bio-optical measurements of chlorophyll fluorescence were made with a Sea Tech fluorometer by Rhea and Davis (1990). Chlorophyll *a* was estimated by fluorescent techniques calibrated by high pressure liquid chromatography (Slagle and Heimerdinger, 1991). Primary productivity was measured by the ^{14}C incubation technique (Knudson *et al.*, 1989; Martin *et al.*, 1993). Nitrate uptake was measured by incubations (McCarthy and Nevins, 1986). Incident PAR (400–700 nm) irradiance was provided by Broenkow *et al.* (1990). Values for the diffuse attenuation coefficient for PAR were reported by Knudson *et al.* (1989) and C. Trees. Records of wind speed and direction, air temperature and relative humidity were extracted from shipboard recording systems on both *Atlantis II* and *Meteor*.

4. THE MODELS

4.1. *The physical model*

The present study and MRM95 utilize a coupled physical and biological model. The physical model is a coupled quasigeostrophic and surface boundary layer (QG–SBL) described by Walstad and Robinson (1993) with algorithmic improvements discussed in McGillicuddy (1993). This model has been used extensively for simulation of the oceanographic environment in many regions of the ocean (Robinson, 1993) including the 1989 JGOFS Bloom Experiment (Robinson *et al.*, 1993). Although the present study deals with a one dimensional representation of this model, the full three dimensional model will be described here. In the following description, the equations for the quasigeostrophic interior are nondimensional while those for the surface boundary layer are presented in dimensional form.

The prognostic equation for the vorticity of the interior fluid is

$$\frac{\partial \zeta}{\partial t} + \alpha J(\psi,\zeta) + \beta\psi_x = F_{pqr} \tag{1}$$

where ψ is the streamfunction and ζ is the dynamic vorticity given by

$$\zeta = \nabla_H^2\psi + \Gamma^2(\sigma\psi_z)_z \tag{2}$$

The Jacobian J is defined as $J(\psi,\zeta) = \psi_x\zeta_y - \psi_y\zeta_x$, the horizontal Laplacian operator is $\nabla_H^2 = \partial^2/\partial x^2 + \partial^2/\partial y^2$ and F_{pqr} represents a Shapiro filter that is used to parameterize subgridscale dissipation. The nondimensional parameters are

$$\alpha = \frac{V_0 t_0}{D} \quad \beta = \beta_0 D t_0 \quad \Gamma^2 = \frac{f_0^2 D^2}{N_0^2 H^2}$$

where the Coriolis frequency and its meridional gradient are defined as

$$f_0 = 2\Omega\sin\Theta_0 \quad \beta_0 = \frac{\partial f}{\partial y}$$

and D, H, t_0 and V_0 are characteristic length, depth, time and velocity scales. The stratification is given by

$$\sigma(z) = \frac{N_0^2}{N^2} \text{ where } N^2 = -\frac{g}{\rho}\frac{\partial \rho}{\partial z}$$

The surface and bottom boundary conditions provide prognostic equations for the top and bottom density:

$$\frac{\partial \Gamma^2\sigma\psi_z}{\partial t} + \alpha J(\psi,\Gamma^2\sigma\psi_z) = \begin{cases} w^1 & \text{at } z = 0 \\ -\kappa\nabla_H^2\psi - J(\psi,b) & \text{at } z = -Z \end{cases} \tag{3}$$

where κ is the bottom friction applied over the topography b. It is through the upper boundary condition that the interior and surface boundary layer models are coupled. The dimensional quasigeostrophic vertical velocity $w^{QG} = V_0 H/f_0 t_0 D\, w^1$ is balanced by the surface boundary layer vertical velocity ω to maintain the rigid lid approximation at the sea surface:

$$w^{QG} + \omega = 0 \text{ at } z = 0 \tag{4}$$

The horizontal Ekman velocities are given by

$$\mu = \frac{\partial}{\partial z}\left(\frac{\hat{j}\cdot\vec{\tau}}{\rho}\right) \nu = -\frac{\partial}{\partial z}\left(\frac{\hat{\imath}\cdot\vec{\tau}}{\rho}\right)$$

with transports

$$\mu_T = \frac{\hat{j}\cdot\tau}{\rho_0 f_0} \nu_T = -\frac{\hat{\imath}\cdot\tau}{\rho_0 f_0}$$

The quasigeostrophic contribution to the total vertical velocity at the surface is

$$w^{QG}(z=0) = \frac{\partial \mu_T}{\partial x} + \frac{\partial \nu_T}{\partial y} - \frac{1}{f_0}(\mu_T R_x + \nu_T R_y) - \frac{\beta_0}{f_0}\nu_T \tag{5}$$

where R is the relative vorticity at the surface

$$R = \frac{V_0}{D}\nabla_H^2\psi|_{z=0}$$

Vertical velocities are assumed to vary linearly with depth in this model. As the boundary

condition sets the surface value, the vertical derivative of the vertical velocity is used to interpolate to the interior component

$$\frac{\partial w^{QG}}{\partial z} = -\frac{V_0\Gamma^2}{f_0 t_0 D}\frac{D}{Dt}(\sigma\psi_z)_z.$$

In this model the bottom of the Ekman layer is taken to be at the base of the mixed layer so ω vanishes there. Thus ω is assumed to vary linearly between $-w^{QG}$ and 0 between $z = 0$ and $z = -h$. Equations for the boundary layer buoyancy, temperature and passive tracer evolution are

$$\rho_t + \alpha(J(\psi^*,\rho) + \mu(\delta^*_x + \rho_x) + \nu(\delta^*_y + \rho_y) + (w^{QG} + \omega)\rho_z) - \frac{\omega}{\Gamma^2\sigma} = (M_\rho)_z + \frac{\alpha_T}{c_p} I_x \tag{6}$$

$$\vartheta_t + \alpha(J(\psi^*,\vartheta) + \mu(\theta_x + \vartheta_x) + \nu(\theta_y + \vartheta_y) + (w^{QG} + \omega)\vartheta_z) - \omega\Theta_z = (M_\vartheta)_z + \frac{1}{c_p} I_z \tag{7}$$

$$\phi_t + \alpha(J(\psi^*, \phi) + \mu(\Phi_x + \phi_x) + \nu(\Phi_y + \phi_y) + (w^{QG} + \omega)\phi_z) - \omega\Phi_z + w_\phi(\phi_z + \Phi_z) = (M_\phi)_z + S_\phi \tag{8}$$

with the quasigeostrophic streamfunction dimensionalized according to

$$\psi^* = V_0 D\psi.$$

The density, temperature and tracer perturbations to the mean profile due to interior motions are

$$\delta^* = \frac{\rho_0 f_0 V_0 D}{gH\sigma}(\sigma\psi_z)|_{z=0} \quad \theta = \frac{V_0 H\Gamma^2}{f_0 D}\Theta_z(\sigma\psi_z)|_{z=0} \quad \phi = \frac{V_0 H\Gamma^2}{f_0 D}\Phi_z(\sigma\psi_z)|_{z=0},$$

where Θ and Φ represent the mean temperature and tracer profiles, respectively. Passive tracers can have arbitrary sinking velocities w_ϕ and source terms S_ϕ. The mixing layer depth equation is

$$h_t + uh_x + vh_y + w = e \tag{9}$$

which must be satisfied at $z = -h$ in the limit approaching from above and below. The entrainment rate e is the flux across the base of the mixing layer. This quantity is derived from the turbulent kinetic energy budget in Garwood's (1977) bulk mixed layer model.

For the present purposes a one dimensional version of the model described above is used. Time dependent mesoscale effects are absent in the one dimensional case, therefore reducing the coupled quasigeostrophic and surface boundary layer physics to the surface boundary layer model with a stationary quasigeostrophic component. In the simulations that follow, the upper 150 m of the water column is discretized into 25 levels of uniform 6 m resolution in the surface boundary layer. The interior contains 12 levels that span the depth interval from the mean depth of 4300 m up to the surface where the QG and SBL grids are nested. The time step is 1.5 hours.

4.2. *The biological model*

A variety of models have been used to simulate the dynamics of upper ocean plankton ecosystems, ranging from the most basic nutrient–phytoplankton–zooplankton models (e.g. Steele, 1974) to much more complex formulations that include dissolved organic material, detritus, bacteria and multiple size classes of organisms (e.g. Fasham *et al.*,

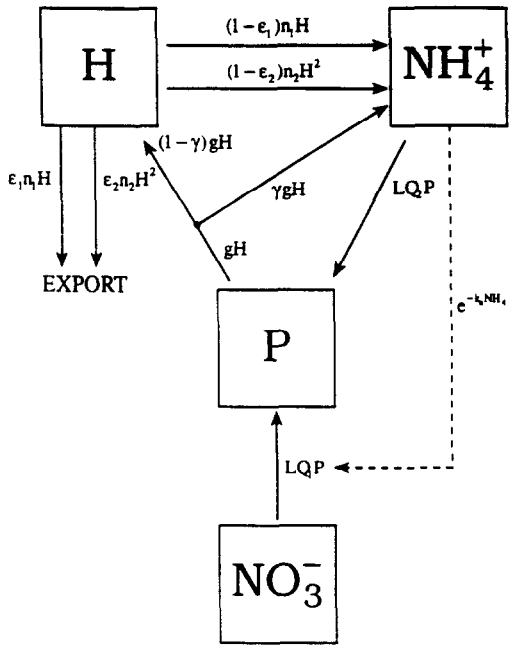

$$L = P_{max}\left(1 - e^{\frac{-PI}{P_{max}}}\right)e^{\frac{-PI}{P_{max}}}$$

$$Q = Q_1 + Q_2 = \frac{NO_3 e^{-k_e NH_4}}{k_1 + NO_3} + \frac{NH_4}{k_2 + NH_4}$$

$$g = R_m(1 - e^{\lambda P})$$

Fig. 3. A schematic diagram of the biological model used in this study.

1990). The approach used here is to keep the model as simple as possible yet to retain enough structure that the basic functioning of the ecosystem is well represented in a framework that is capable of exposing the processes of interest—namely the effects of mesoscale and upper ocean dynamics on biological productivity. A nitrogen based nutrient–phytoplankton–heterotroph model is introduced that is intermediate in complexity with respect to the two models cited above. For the purposes of investigating how physical transports supply nutrients to the euphotic zone it is particularly useful to treat new and regenerated forms of nitrogen separately. This facilitates explicit distinction between primary production that results from the injection of nitrate from below and that which is sustained on recycled ammonium.

A schematic diagram of the biological model is shown in Fig. 3. The model equations for phytoplankton (P), heterotrophs (H), nitrate (NO_3^-), ammonium (NH_4^+) and exported nitrogen (N_E) are

Table 1. *Biological model parameters and definitions*

Parameter	Description
k_w	light attenuation due to water
k_c	phytoplankton self shading parameter
p_{max}	maximum photosynthetic rate
p_1	initial slope of photosynthesis response to light
p_2	photoinhibition parameter
k_1	half saturation constant for nitrate uptake
k_2	half saturation constant for ammonium uptake
k_n	strength of ammonium inhibition of nitrate uptake
R_m	maximum grazing rate
Λ	Ivlev constant
γ	grazing efficiency
n_1	linear heterotrophic loss rate
n_2	quadratic heterotrophic loss rate
ε_1	exported fraction of linear heterotrophic loss rate
ε_2	exported fraction of quadratic heterotrophic loss rate
w_{sink}	phytoplankton sinking rate
f_w	f-ratio dependence of phytoplankton sinking rate

$$\frac{\partial P}{\partial t} = LQP - gH \tag{10}$$

$$\frac{\partial H}{\partial t} = (1 - \gamma)gH - n_1H - n_2H^2 \tag{11}$$

$$\frac{\partial \mathrm{NO_3}}{\partial t} = -LQ_1P \tag{12}$$

$$\frac{\partial \mathrm{NH_4}}{\partial t} = -LQ_2P + \gamma gH + (1 - \varepsilon_1)n_1H + (1 - \varepsilon_2)n_2H^2 \tag{13}$$

$$\frac{\mathrm{dN_E}}{\mathrm{d}t} = \varepsilon_1 n_1 H + \varepsilon_2 n_2 H^2 \tag{14}$$

The model parameters are listed in Table 1. The first four equations describe the local tendencies of the various nitrogen constituents that result from biological processes. Because these species of nitrogen are to be incorporated as passive tracers in a four dimensional physical model of the ocean, these partial derivatives represent only part of the overall local tendency which is affected by physical processes as well. The local tendencies are used as forcing functions S_ϕ in the tracer evolution equations of the coupled quasigeostrophic and surface boundary layer model. The complex nonlinearity of the biological equations requires that they be solved numerically. A fourth order Runge–Kutta technique with adaptive stepsize control (Press *et al.*, 1986) is used in the present work to solve equations (10–13). The transport of exported nitrogen by ocean currents is not treated. This material is assumed to sink instantaneously to the deep ocean and is accumulated in a two dimensional (x,y) model sediment trap whose time evolution is given by equation (14).

Phytoplankton growth is both light and nutrient limited. The photosynthetic response to irradiance is

$$L = P_{max}\,(1 - e^{-p_1 I/P_{max}})\,e^{-p_2 I/P_{max}}$$

following the formulation of Platt *et al.* (1980). The light field is affected by phytoplankton pigments through self shading. Their effect on the inherent optical properties of the water column is given by

$$I(x,y,z,t) = I_0(t)e^{k_w z + k_c \int_0^z P(x,y,z,t)\mathrm{d}z}$$

The maximum specific rate of growth L for a given light intensity is modulated by a nutrient limitation factor Q similar to the one used by Fasham *et al.* (1990):

$$\begin{aligned} Q &= Q_1 + Q_2 \\ &= \frac{NO_3\, e^{-k_u NH_4}}{k_1 + NO_3} + \frac{NH_4}{k_2 + NH_4} \end{aligned}$$

It is composed by both nitrate and ammonium components which are cast in the familiar Michaelis–Menten form commonly used to represent nutrient uptake. This formulation first proposed by Wroblewski (1977) allows for the commonly observed ammonium inhibition of nitrate uptake that results from the phytoplankton preference for the reduced form of nitrogen. The total phytoplankton sinking rate w_P is the sum of a constant rate and a term that depends linearly on the f-ratio

$$w_P = w_{sink} + f \cdot f_w$$

where the f ratio is defined as

$$f = \frac{Q_1}{Q_1 + Q_2}$$

The f-ratio dependence can in some cases be used to parameterize the effect of a shift in species composition. For example, early in a spring bloom a phytoplankton assemblage dominated by large diatoms that sink rapidly once the nutrients are depleted would give rise to a high f-ratio. Later in the bloom, when the large diatoms have been replaced by smaller flagellated species that sink much more slowly, the f-ratio would decline. Numerical experiments will show that this process is not crucial to the evolution of the biological and chemical properties of the water column in these bloom simulations. However this effect will be retained in the model for consistency in the presentation of results. Note that the sinking rate does not appear in the biological equations because it is a transport that is dealt with in the physical model (equation 8).

Heterotrophic consumption of phytoplankton biomass is represented by Ivley's (1955) grazing function:

$$g = R_m(1 - e^{-\lambda P})$$

which has been studied and used extensively in modeling applications (Parsons *et al.*, 1984; Mullin *et al.*, 1975; Steele and Mullin, 1977). The parameter γ determines the efficiency with which the grazed material is assimilated into heterotrophic biomass. The heterotrophic loss rate has both linear and quadratic terms. The quadratic form first suggested by Steele and Henderson (1981) is an effective way to parameterize the predation of herbivores by carnivores. Loss via this mechanism is quite small at low herbivore concentrations but dominates heterotrophic loss at higher abundance. This behavior

proves to be critical in maintaining stability in the balance between phytoplankton and heterotrophs in cases when the rate of grazing approaches the rate of phytoplankton growth. Heterotrophic losses are partitioned into recycled and exported components by the two parameters ε_1 and ε_2.

Detritus is not treated explicitly in this model. Regeneration of the nitrogen content of this material is assumed to occur instantaneously. Alternatively, this assumption can be interpreted that the detrital nitrogen pool is in steady state, so inputs and outputs balance each other. Care must be taken in applying this model to situations where significant changes in detrital nitrogen occur. For example, while ignoring detrital accumulation early in a spring bloom simulation is probably justifiable, it may be less appropriate in the late-bloom and post-bloom context. However, for the present purposes of investigating the basic processes of physical–biological interactions, this is not likely to be a critical omission. Furthermore, because the relevant fluxes into and out of the detrital reservoir are not well known nor quantified by experimental measurements, the interpretive power gained by additional complexity is of questionable value in this case.

5. MODEL INITIALIZATION

The model is initialized with profiles of buoyancy and temperature that are homogeneous in the mixed layer and linearly stratified below. There is no discontinuity at the base of the mixed layer. These profiles are fitted to the available data as described below. The nitrate profile is defined through a linear relationship with σ_T. Distributions of phytoplankton, heterotrophs and ammonium are assumed to be homogeneous and low in the initial condition (0.5, 0.04 and 0.02 μM nitrogen units, respectively).

Care must be taken to ensure that a single linear nitrate–σ_T relationship is appropriate. Figure 4 shows the ensemble of all upper ocean nitrate measurements plotted as a function of σ_T. This distribution of points appears to represent two linear portions that intersect at $\sigma_T = 27.0$. This intersection lies at the surface σ_T value measured at the beginning of the experiment. Hence the change in slope for $\sigma_T < 27.0$ is representative of a perturbation to the mean linear profile by heating and phytoplankton uptake near the surface. Because the nitrate–σ_T relationship is roughly linear for $\sigma_T > 27.0$ over the range of observed water masses, it is assumed that this single linear relationship is appropriate for initialization purposes. This relationship yields a surface nitrate concentration of 5.8 μM outside the eddy on day 115, which is consistent with the data. It predicts a surface nitrate concentration of 8.4 μM inside the eddy on day 115, where no data are available.

The top row of Fig. 5 shows the initial model buoyancy, temperature and nitrate profiles and data from the first three days of observations outside the Small eddy (days 115–117). These data are chosen to be representative of the background state with no eddy perturbation. It can be argued that these observations do not necessarily reflect the true background state because the observations lie in the submesoscale anticyclone (Fig. 2a). However, the strength of this feature is known to be weak relative to the magnitude of the Small eddy perturbation. Therefore, this ensemble of measurements can be reasonably expected to reflect the background state.

Data are available inside the Small eddy only for the latter part of the experiment, so initial upper ocean profiles must be inferred for this region. Here mesoscale perturbations are represented by vertical displacements of the mean stratification, which is linear. If the mixed layer depth is assumed to be spatially uniform on the mesoscale, then eddy

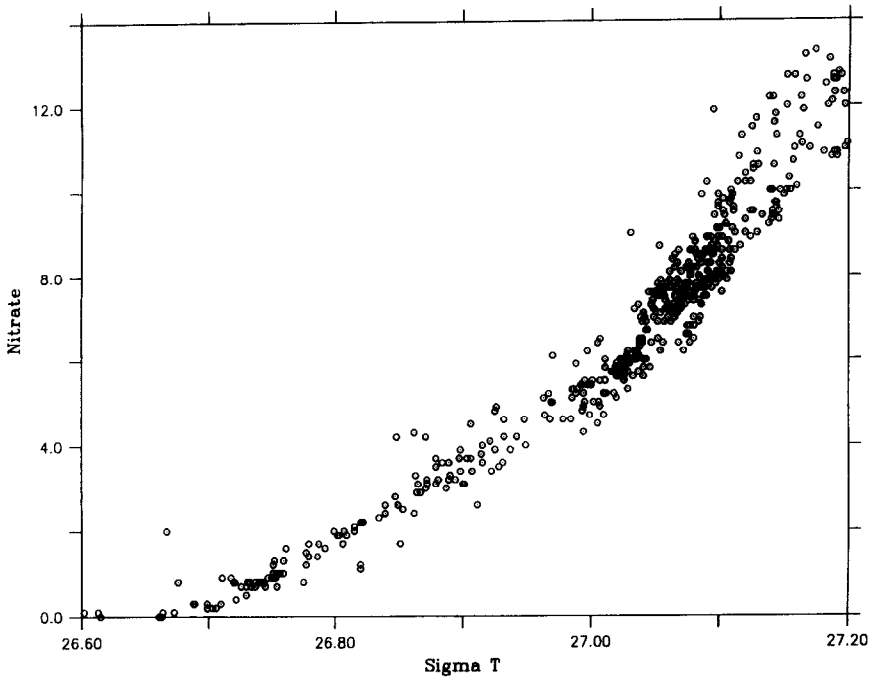

Fig. 4. Upper ocean nitrate concentrations (μM) plotted as a function of σ_T.

perturbations simply shift profiles along the abscissa. A number of authors have shown that mesoscale eddies can induce spatial variability in the depth of the mixed layer (Klein and Hua, 1988; Stevenson, 1983; Walstad and Robinson, 1993). However, the root mean square variation is generally less than 10%, so mesoscale variability in the initial mixed layer depth will not be included in this analysis.

The initial conditions used inside the Small eddy are shown in Fig. 5 (bottom row). Exactly the same initialization parameters have been used. The only difference is that the profiles have been shifted by an amount consistent with the perturbation of the Small eddy. The vertical gradient below the mixed layer appears to be less than in the top row because the profiles are plotted on different scales. The data were collected much later in the experiment (days 142–151) so it is expected that the model initial condition should be quite different from these observations near the surface where significant heating and nutrient uptake have occurred. However, it is important to note that the profiles do agree at depth, where modification due to surface processes are negligible. This suggests that the initial condition is in fact satisfactorily tuned to the data.

6. ESTIMATION OF THE BIOLOGICAL MODEL PARAMETERS

6.1. *The light environment*

The equation for the total light extinction coefficient for photosynthetically active radiation k_{par} is

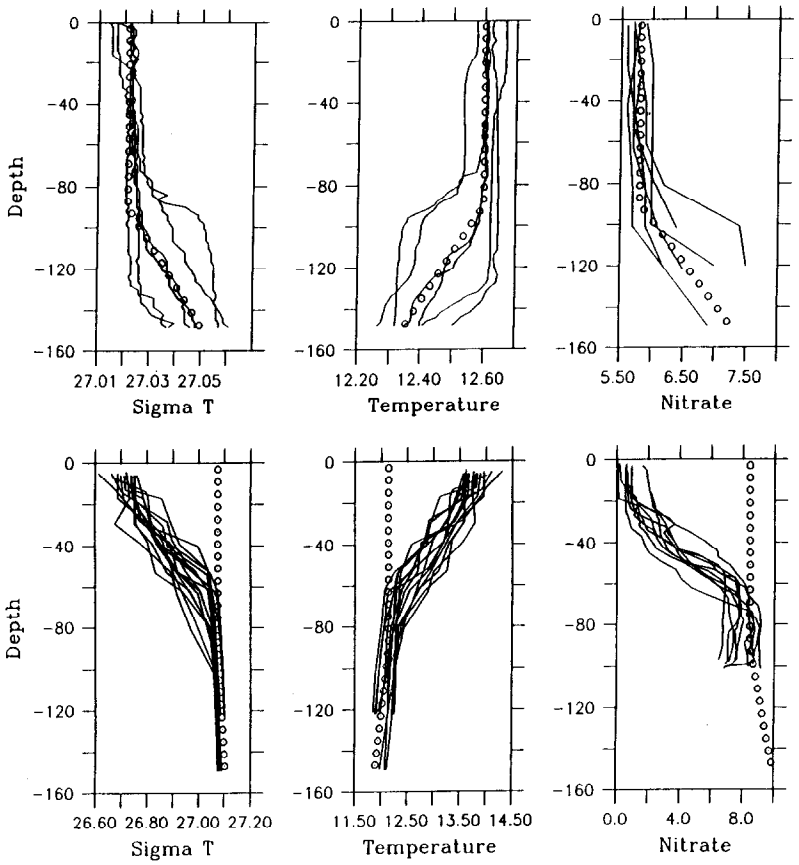

Fig. 5. Initial profiles of σ_T, temperature and nitrate for outside the Small eddy (top row) and inside the Small eddy (bottom row). Values used to initialize the model are indicated as open circles. Data collected on days 115–117 outside the Small eddy are shown as solid lines in the top row. Data collected on days 142–151 inside the Small eddy are shown as solid lines in the bottom row. Note that the abscissa scales of the top row are much narrower than those of the bottom row.

$$k_{par} = k_w + k_c P$$

where k_w is the coefficient for pure seawater and k_c is a phytoplankton self shading parameter. Observed changes in phytoplankton abundance and the light field from days 115–128 were used to estimate the light environment parameters. Bio-optical measurements indicate phytoplankton biomass approximately tripled over this time period. In nitrogen units, this corresponds to P varying from its initial value 0.5–1.5. Meanwhile, the average k_{par} increased from 0.07 to 0.11. The best estimates for k_w and k_c are thus the solutions to the matrix equation

$$\begin{bmatrix} 1.0 & 0.5 \\ 1.0 & 1.5 \end{bmatrix} \begin{bmatrix} k_w \\ k_c \end{bmatrix} = \begin{bmatrix} 0.07 \\ 0.11 \end{bmatrix}$$

which is simply

$$\begin{bmatrix} k_w \\ k_c \end{bmatrix} = \begin{bmatrix} 0.05 \\ 0.04 \end{bmatrix}$$

This value of k_w is slightly higher than the estimate of 0.04 made by Lorenzen (1972) and used by Fasham *et al.* (1990). The value of k_c is also slightly higher than some published values (Fasham *et al.*, 1983; Kirk, 1983) and that used by Fasham *et al.* (1990), but well within reasonable bounds due to the uncertainty in phytoplankton nitrogen biomass determination. Although these coefficients are somewhat different from what has been used by previous authors, they do yield a simulated underwater light field that is consistent with observations (see Figs 16b, 24b and discussion below).

6.2. *Phytoplankton parameters*

The most important aspect of the phytoplankton growth rate expression is the photosynthesis versus irradiance relationship. The primary production measurements are useful in determining two of the three relevant parameters of this function. The ^{14}C incubations are a measure of the total carbon uptake over the dawn to dusk incubation period. The total amount of carbon assimilation depends not only on the photosynthesis versus irradiance function, but also the phytoplankton biomass inside the experimental container. Because the actual phytoplankton biomass inside the container is not known with sufficient certainty, it is impossible to determine specific rates of photosynthesis accurately. However, normalizing each primary production profile to its maximum value allows the estimation of the light dependent photosynthesis parameters p_1 and p_2. Figure 6 shows the normalized profiles and the chosen model fit to the data. Care must be taken in the interpretation of the normalized profiles because on those days in which there was not enough light to saturate the photosynthetic apparatus of the upper samples, the profiles will be normalized to something less than $P_{\max}$ and therefore the initial slope will be overestimated. Therefore the model representation was subjectively chosen to fit those profiles which show distinguishable saturation at higher light intensities. Although two data points indicate some photoinhibition, this is not thought to be a critical process in the context of the present study and p_2 was set to zero.

Because no measurements of the maximum specific growth rate are available for this data set, this parameter was set to a value that produced nutrient removal, phytoplankton biomass and primary productivity that are consistent with the data. The chosen value (0.66 day^{-1}) falls within the range of estimates derived from field and laboratory measurements (Parsons *et al.*, 1984) although it may be slightly low for a bloom situation.

There are relatively few published half saturation values for ammonium and nitrate uptake characteristic of natural assemblages of oceanic versus coastal or estuarine phytoplankton (see review by Goldman and Glibert, 1983). For ammonium these range from undetectable to 0.6 μM and from 1.1 to 1.3 μM in low and high nutrient oceanic regions, respectively. For nitrate they range from undetectable to 0.9 μM and from 1 to 4.2 μM in low and high nutrient oceanic regions, respectively. The assessment of half saturation constants for nutrient uptake during this experiment was particularly difficult because nitrate and ammonium uptake rates were saturated at the ambient concentrations observed throughout most of the period of observation. Approximations of ammonium half saturation constants were very low (less than 0.02 μM) with large uncertainties because of the common condition of near saturating levels of substrate. Due to these

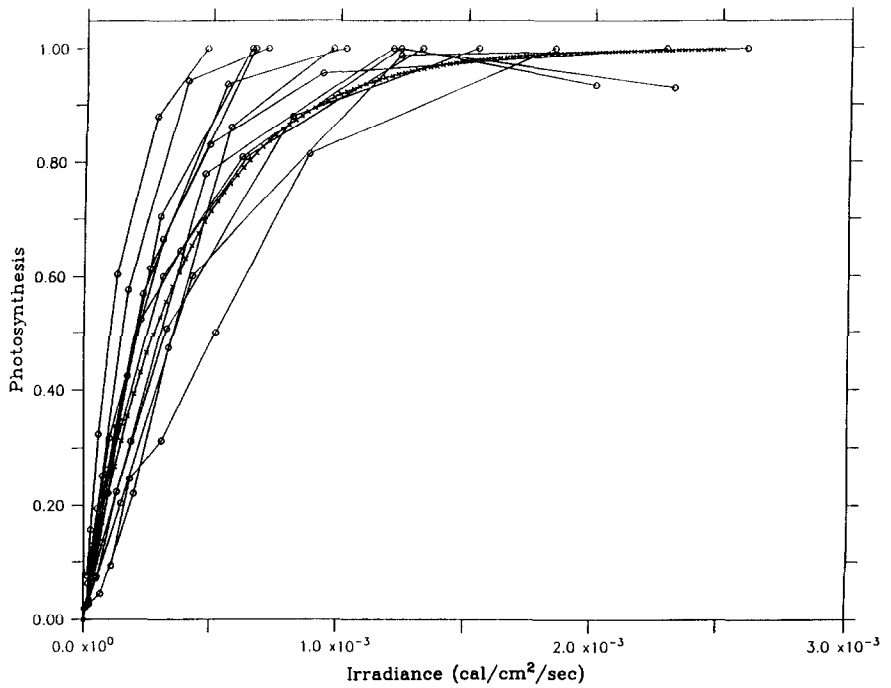

Fig. 6. The model representation of the light dependence of the photosynthesis versus irradiance data (see text). Normalized photosynthesis versus irradiance curves from the Leg 2 primary production measurements are shown as open circles connected with solid lines. The cross-hatched line is the model curve.

considerations and in the absence of other data from this specific study region, we believe that relatively low half saturation constants, 0.05 and 0.2 μM for ammonium and nitrate uptake, respectively, are justified for modeling purposes.

While many laboratory, coastal and estuarine, as well as some oceanic data sets indicate nearly complete suppression of phytoplankton nitrate uptake when ammonium concentrations exceed about 1 μM (see, for example, Syrett, 1981; McCarthy, 1981), the experiments conducted during this study indicate much greater sensitivity of nitrate uptake to ammonium presence. Another region that has revealed a similar pattern is the subarctic Pacific (Wheeler and Kokkinas, 1990). These investigators found that concentrations as low as 0.1 μM could completely suppress nitrate uptake. Similar results in the present study are shown in Fig. 7, where very little nitrate uptake occurs for concentrations of ammonium in excess of 0.1 μM even though nitrate availability is in excess of saturating concentrations. Based upon these data an e-folding concentration of ammonium for nitrate uptake was set at 0.1 μM in the model.

There are no measurements of the phytoplankton sinking rate available for this experiment. Values for w_{sink} and f_u were chosen that produced phytoplankton biomass distributions that are consistent with the data. As discussed in the model formulation, the dependence of the sinking rate on the *f*-ratio is an attempt to parameterize the effect of changing species composition. Early in the bloom when the *f*-ratio is high, sinking rates can approach 5.5 m/day, which is a conservative yet reasonable rate for fast sinking diatoms

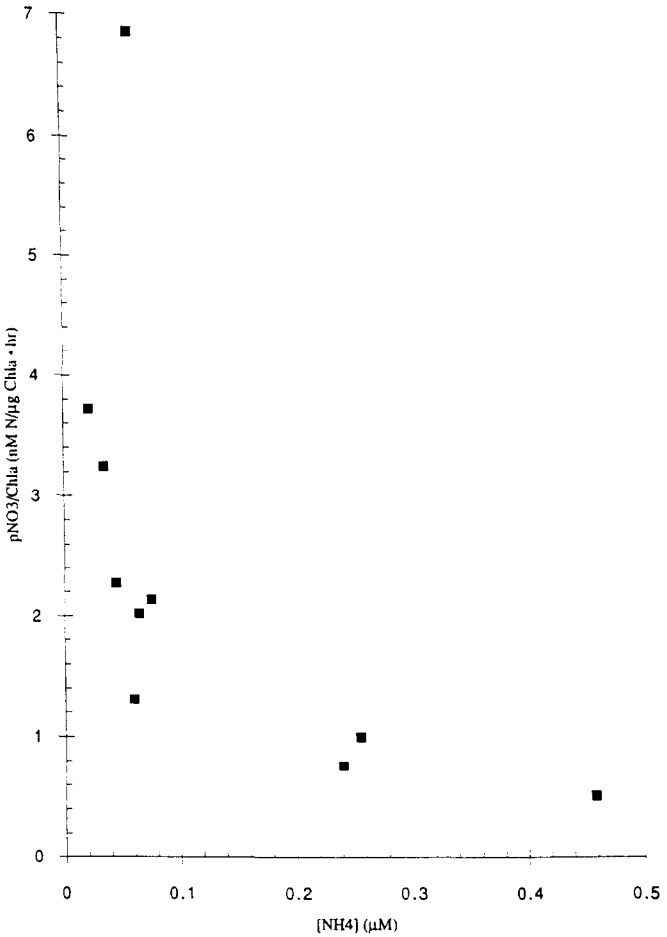

Fig. 7. Nitrate uptake plotted as a function of ammonium concentration. Nitrate uptake values have been normalized to the chlorophyll *a* of the sample. The data show strong ammonium inhibition of nitrate uptake for concentrations greater than 0.1 μM.

known to predominate during that time. Sinking rates up to 100 m/day have been reported in the literature (Alldredge and Gotschalk, 1989). As the *f*-ratio falls later in the bloom, sinking rates can decrease to as little as 0.5 m/day which is more characteristic of sinking rates reported for non-bloom situations (Bienfang, 1981).

6.3. *Heterotroph parameters*

Recent evidence suggests that microzooplankton are the dominant grazers of phytoplankton populations in open ocean environments (e.g. Capriulo, 1990). In fact, observations during the NABE indicate that mesozooplankton exerted only slight grazing pressure on phytoplankton, consuming only a few percent of the total primary production (Dam *et al.*, 1993). Heterotrophic parameters were therefore chosen to represent herbivorous microzooplankton, with a maximum growth rate approaching that of phytoplankton. Unfortunately no direct grazing measurements are available for this ensemble

Table 2. Biological model parameter values

Parameter	Units	Value
k_w	m^{-1}	0.05
k_c	$m^{-1}\mu M^{-1}$	0.04
p_{max}	day^{-1}	0.66
p_1	$(cal^{-1}\ cm^2)^{-1}$	0.0019
p_2	$(cal^{-1}\ cm^2)^{-1}$	0.0
k_1	μM	0.2
k_2	μM	0.05
k_n	μM	27.2
R_m	day^{-1}	0.69
Λ	$(\mu M)^{-1}$	1.0
γ	nondimensional	0.25
n_1	day^{-1}	0.11
n_2	day^{-1}	0.52
ε_1	nondimensional	0.75
ε_2	nondimensional	0.50
w_{sink}	m day^{-1}	0.5
f_w	m day^{-1}	5.0

of organisms during the experiment, so values of R_m, Λ and γ were chosen to be consistent with the range of previously reported values. Little is known about the loss rates of these organisms and how the loss is partitioned into recycled and exported material. Thus n_1, n_2, ε_1 and ε_2 were tuned to maximize agreement between the model and available data.

6.4. *Summary*

Of the 17 biological model parameters, only four (k_c, p_1, p_2 and k_n) are well constrained by measurements during the NABE and three (k_w, k_1 and k_2) by values reported in the literature. The literature provides some guidance for the remaining 10 parameters, but not all. With these caveats in mind, the unknown model parameters were tuned within reasonable ranges in order to best represent the data. Several hundred runs were carried out and the best fit to the data was chosen subjectively. The "best fit" parameter values used in the simulations that follow are listed in Table 2.

7. ONE DIMENSIONAL SIMULATIONS

In the following one dimensional simulations the physical model is forced by surface fluxes of heat and momentum estimated from shipboard meteorological observations and standard bulk formulae (Gill, 1982). Figure 8 shows the records of wind and insolation and the computed surface heat flux (comprising sensible, latent and longwave radiative fluxes). A comparison of the model simulated mixed layer depth with observations is shown in Fig. 9. A variety of criteria have been proposed for the determination of the mixed layer depth. In this case it has been subjectively chosen as the shallowest depth where significant stratification exists. The model captures the general features of the mixed

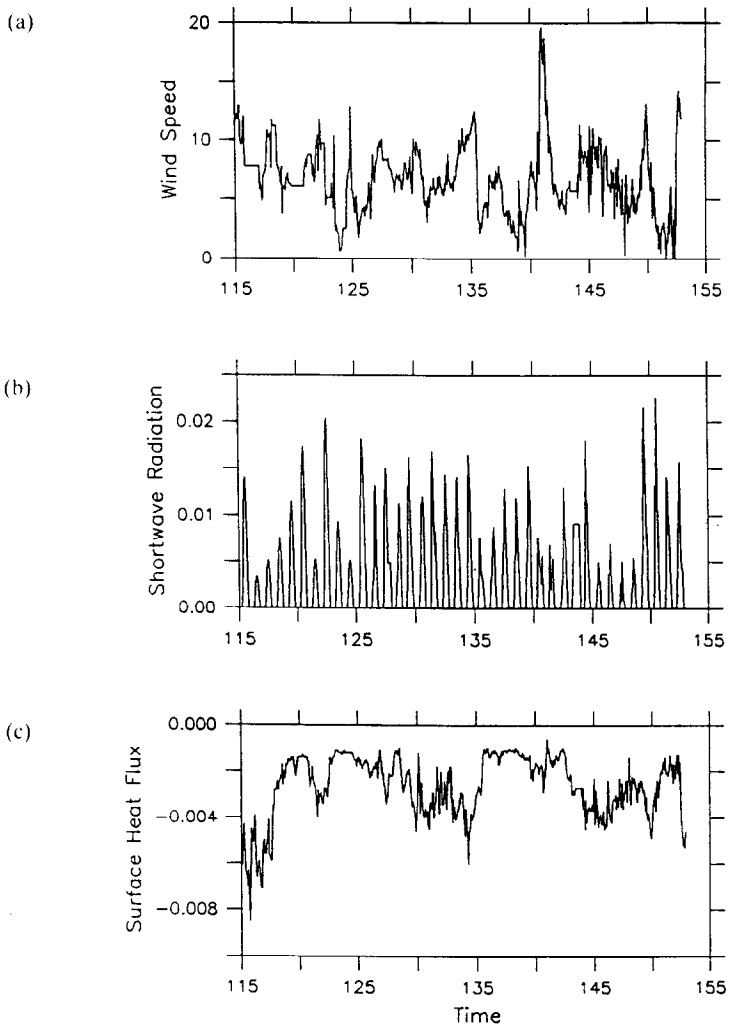

Fig. 8. Time series of quantities used to force the physical model: (a) wind speed (m s^{-1}), (b) shortwave radiation (cal cm^{-2}) and (c) surface heat flux (cal cm^{-2}).

layer depth time series, including the shoaling that occurs during the onset of stratification, high frequency (hours to days) fluctuations and the storm event on day 142. Clearly these features are not perfectly represented by the model. The initial stratification is more intermittent in the model than the data suggest. In general the model seems to convect to a greater depth at night than is indicated by the data. The mixed layer does not deepen enough during the storm. However, the model employed here is a simple bulk model that cannot represent all of the complex structure observed in the ocean. It does, however, capture the general features of the mixed layer and seasonal thermocline system (see below) relevant to the biological processes of interest. Sensitivity analyses indicate that the biological simulations are reasonably robust with respect to the detailed behavior of the mixed layer.

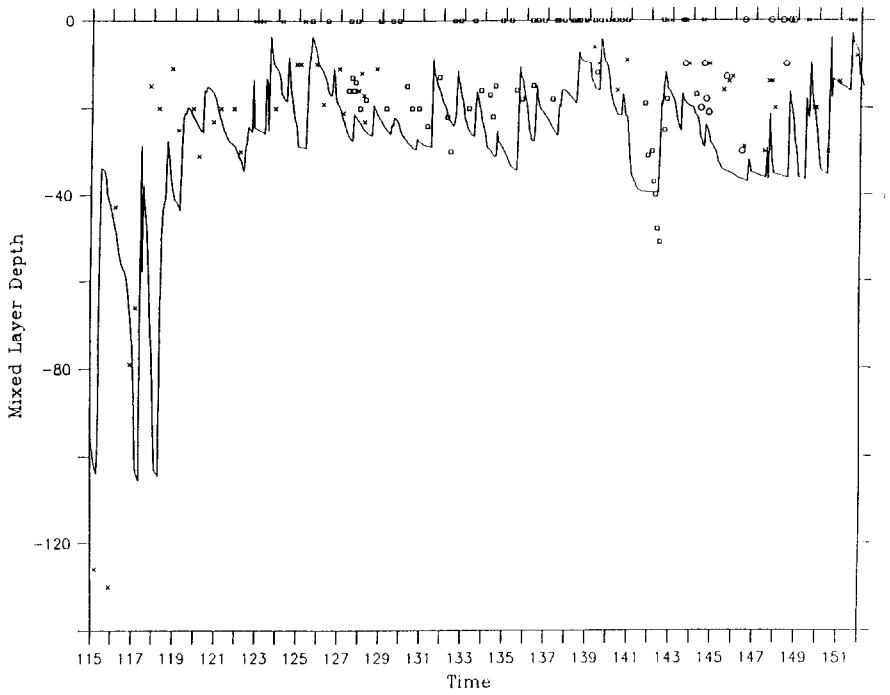

Fig. 9. Observations of mixed layer depth from CTD casts (crosses: *Atlantic II*; squares: *Meteor*; circles: *Discovery*) and simulated mixed layer depth (solid line). The mixed layer depth is reported to be zero when no clearly definable homogeneous layer exists in the temperature and salinity profiles.

7.1. *Early/Outside*

Time series of simulated and observed temperature profiles are shown in Fig. 10. The data reveal a water column initially well mixed to a depth of 100 m which quickly stratifies as heat is pumped into the near surface region. Surface temperatures rise from 12.4°C to approximately 13.0°C. However, there are significant temperature fluctuations below the upper 50 m or so that is directly forced by the surface heat flux. The fairly dramatic lifting of temperature surfaces toward the end of the observations suggests the presence of mesoscale and/or submesoscale variability. Analysis of the cruise track in relation to the mesoscale and submesoscale environment (Fig. 2c) suggests that the ship did in fact traverse physically distinct features. Observations for this leg commenced on day 115 in a submesoscale warm feature to the west of the Small eddy. Days 117–120 were spent in the frontal region between the warm feature and the western flank of the small eddy. The ship then moved to the cold feature to the west of the submesoscale anticyclone during days 121–125. Finally, days 126 through 128 were spent in the frontal region between the anticyclone and the Small eddy. In fact, these measurements were collected further to the east than the previous stations in the frontal region. Their proximity to the interior of the Small eddy accounts for the apparent cooling at depth shown in the data.

Figure 10a shows the model evolution of the temperature profile. Of course the mesoscale and submesoscale variability are not represented in the one dimensional model. However, the general features of the temperature evolution shown in the data are

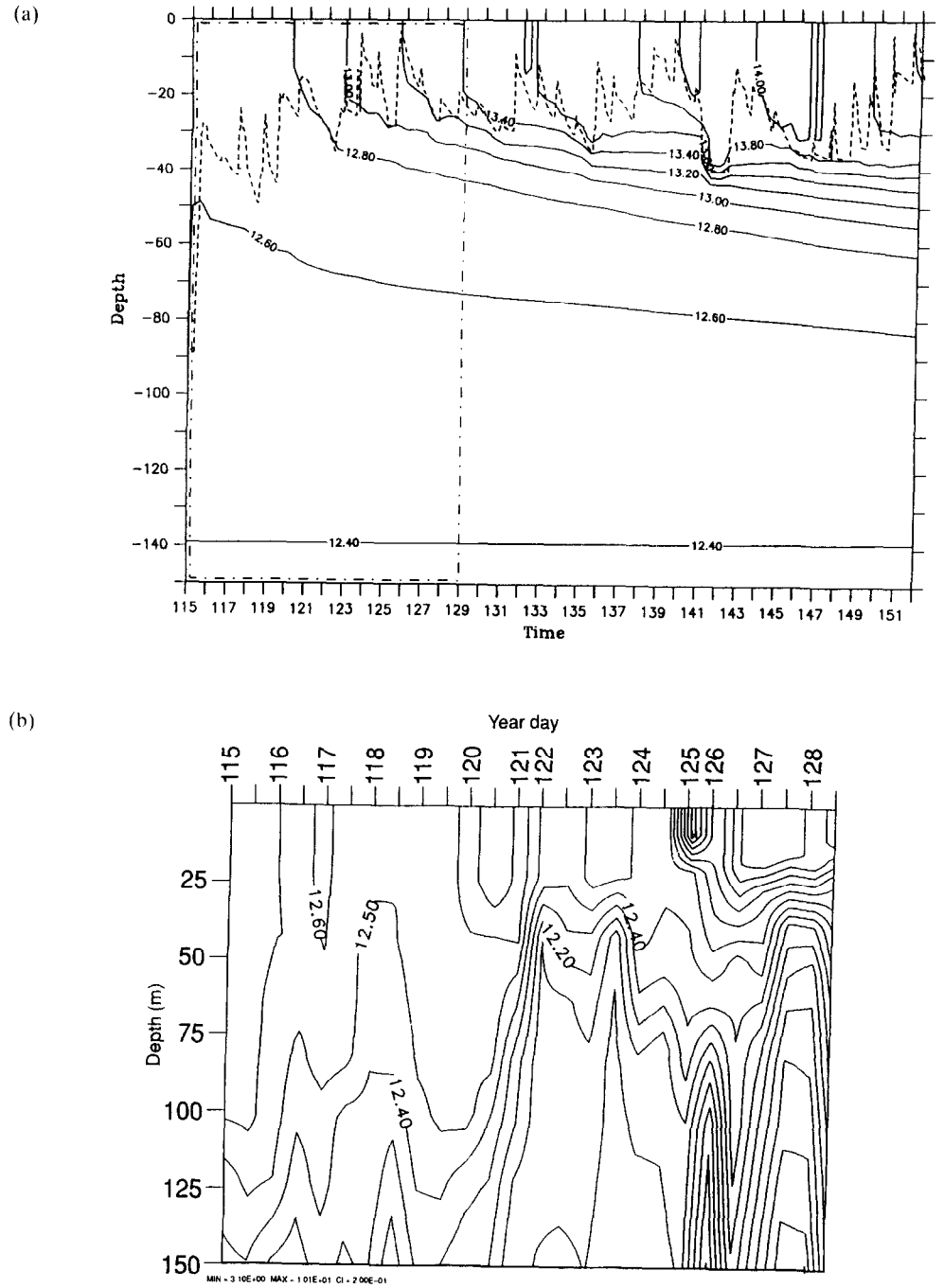

Fig. 10. (a) The evolution of the temperature profile for the Early/Outside simulation. The dashed line indicates the location of the mixed layer depth during time series. The dashed–dotted line denotes the extent of the data shown in (b). In (b) the spacing between days appears to vary because the contouring algorithm spaces the casts regularly and some days have multiple casts while others do not.

captured. The surface temperature rises to approximately 13.4°C, slightly higher than is observed. But, the fact that the ship moved toward a cold feature at the end of the observational period could account for this difference. By day 128 a seasonal thermocline has begun to form between 20 and 40 m, which is roughly consistent with the data.

Figure 11a shows the evolution of the model nitrate profile. Nitrate is removed from the surface layer more quickly than in the data (Fig. 11b). Surface values on day 128 are 2.2 μM and 3.2 μM, respectively. This discrepancy is attributable to mesoscale variability according to the following argument. The difference in initial surface nitrate concentration between inside versus outside the Small eddy was estimated to be 3 μM (Fig. 5). A bias in the observations toward sampling colder more nutrient rich features at the end of the time series could therefore account for the difference; moving from a warm feature into a colder one causes an apparent supply of nitrate. Given the fact that the difference is only one third of the expected variation between the exterior of the eddy and its inner core, this is certainly plausible. It is also possible that errors in the model nitrate uptake rate could account for some of the discrepancy near the surface. However, the observed increase in nitrate below the euphotic zone (Fig. 11b) is highly suggestive of mesoscale variability. MRM95 show that the discrepancy can be reconciled with a three dimensional model. By sampling the four dimensional model nitrate field in space and time along the cruise track, the model can be brought into near perfect agreement with the data.

Figure 12a shows the evolution of the model phytoplankton nitrogen profile. Phytoplankton begin to accumulate in the near surface region soon after the mixed layer shoals. The rate of accumulation appears to be somewhat higher than that indicated by bio-optical measurements of chlorophyll (Fig. 12b) assuming a chlorophyll to nitrogen ratio of 1 g Chl*a*:1 mol NO_3 (Marra and Ho, 1993). By day 128, the model surface value is approximately 2.5 μM, which is not statistically different from the observations given the potential variation in the chlorophyll to nitrogen ratio. It is possible that temporal changes in the chlorophyll to phytoplankton nitrogen ratio may be partially responsible for the apparent difference in biomass accumulation. However, no discernible trend is evident in this ratio when computed from the bulk particulate nitrogen data (not shown). Variations in the chlorophyll to phytoplankton nitrogen ratio with depth due to photoadaptation might account for some of the vertical structure in the data that are not captured by the model. But, again it is not possible to identify a trend from the samples of bulk particulate nitrogen.

A comparison of simulated primary productivity profiles with data from *in situ* ^{14}C incubations is shown in Fig. 13. A constant carbon to nitrogen ratio of 6.7 has been used to make this comparison. Early in the time series there is a systematic underestimation of primary production by the model in the near surface region. However, later in the time series (days 123–128) agreement is much better. We have been unable to formulate a satisfactory explanation for why the model is overpredicting phytoplankton biomass and underpredicting productivity early in the simulation. It is possible that the phytoplankton carbon to nitrogen ratio might have changed during this time period. Analysis of the time series of this ratio in particulate organic matter reveals a great deal of variability but no statistically significant trend (not shown). Alternatively, it may be that changes in species composition caused a shift in the photosynthetic rate parameters. The data do not indicate a consistent trend in either p_1 or p_2 but changes in p_{max} cannot be ruled out.

The evolution of the model heterotrophic population is shown in Fig. 14. Unfortunately there are no microzooplankton measurements with which to compare this time series. The

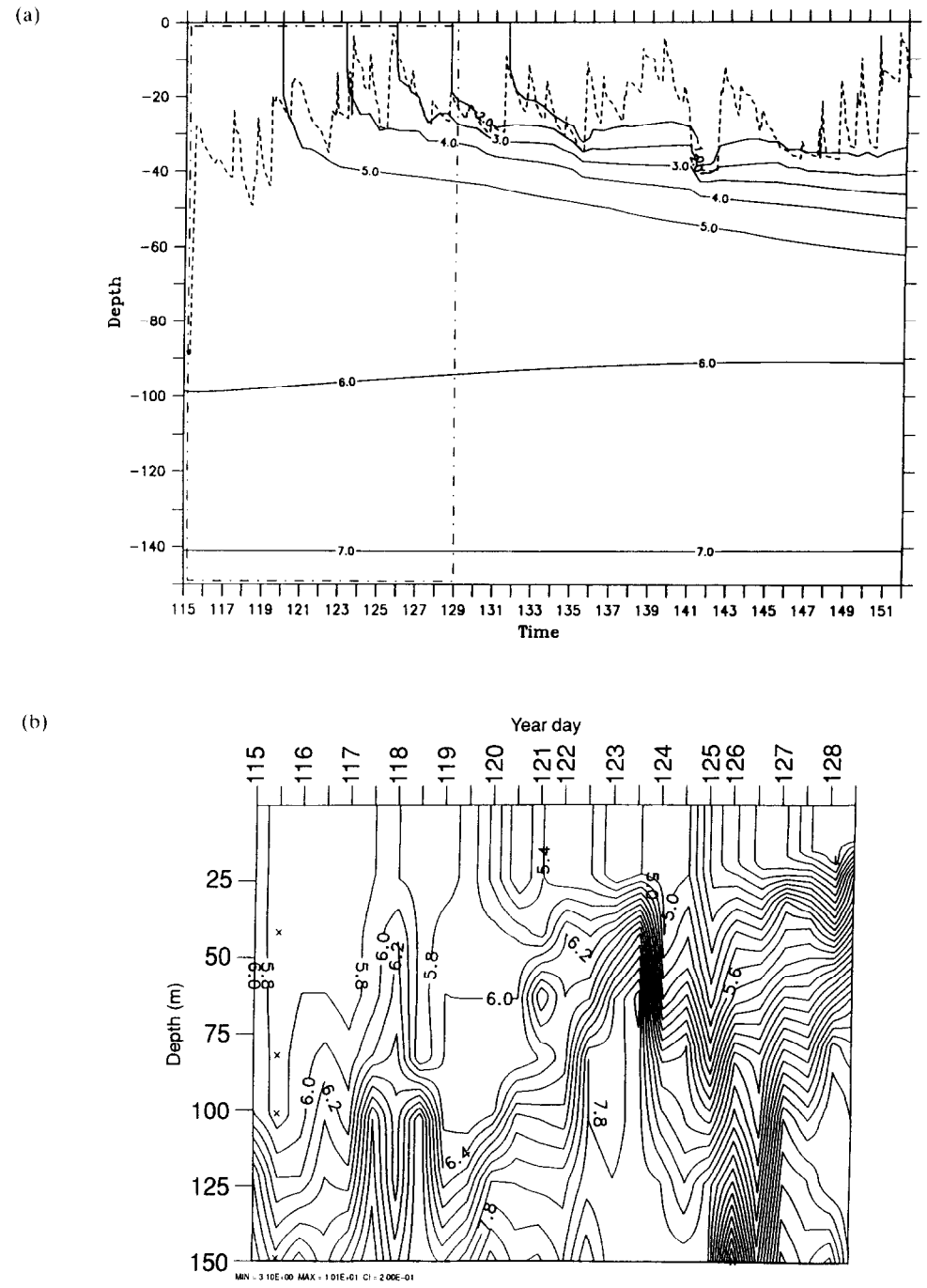

Fig. 11. (a) The evolution of the nitrate profile for the Early/Outside simulation. The dashed line indicates the location of the mixed layer depth during the time series. The dashed–dotted line denotes the extent of the data shown in (b). In (b) the spacing between days appears to vary because the contouring algorithum spaces the casts regularly and some days have multiple casts while other do not.

(a)

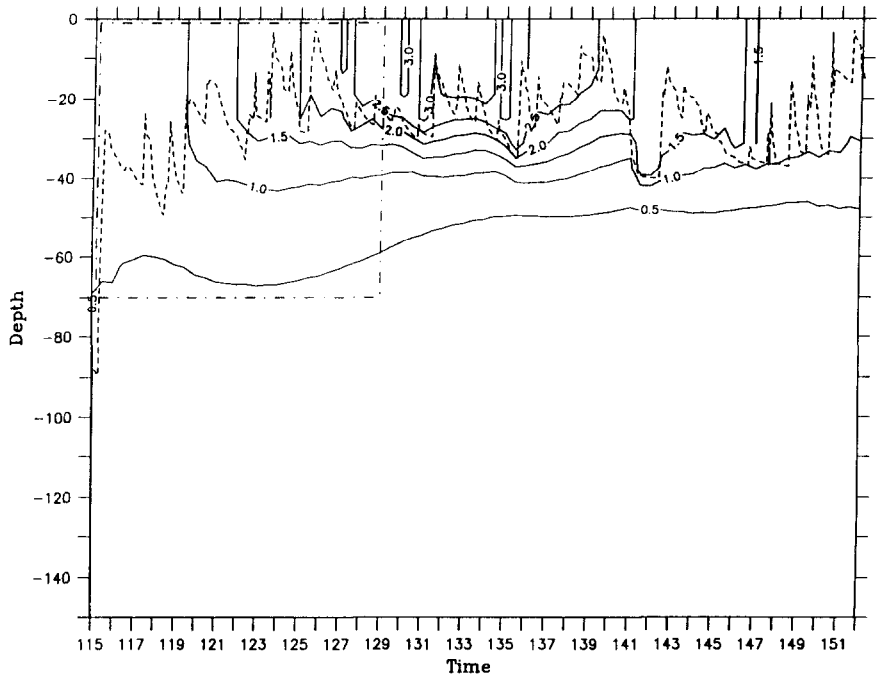
Depth
Time
0
-20
-40
-60
-80
-100
-120
-140
115 117 119 121 123 125 127 129 131 133 135 137 139 141 143 145 147 149 151
0.5
1.0
1.5
2.0
3.0

(b)

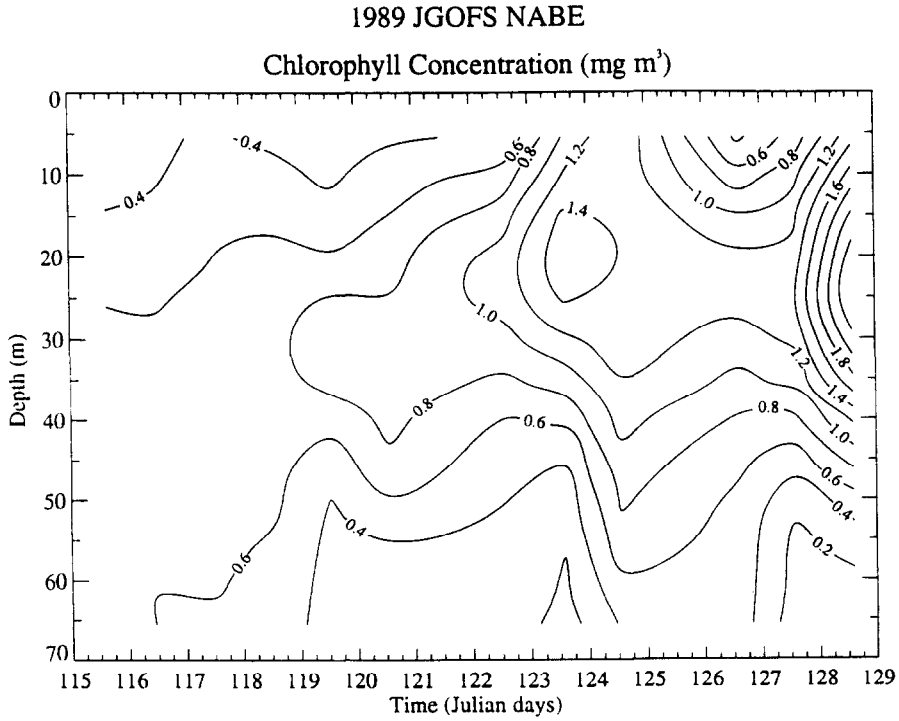
1989 JGOFS NABE
Chlorophyll Concentration (mg m³)
Depth (m)
Time (Julian days)
0
10
20
30
40
50
60
70
115 116 117 118 119 120 121 122 123 124 125 126 127 128 129
0.2
0.4
0.6
0.8
1.0
1.2
1.4
1.6
1.8

model generates a bloom in the heterotrophic population that is closely coupled to the phytoplankton crop. Peak values occur at approximately the same time (day 135). The vertical distribution of heterotrophs is similar to the phytoplankton in that abundance is greatest in the mixed layer and decreases rapidly below the euphotic zone. Some decrease in heterotropic abundance with time is evident in the deepest layers due to mortality.

The evolution of the model ammonium profiles is shown in Fig. 15. No ammonium measurements were made during this time outside the eddy. However, the presence of a strong subsurface ammonium maximum is consistent with the observations made later inside the eddy (see below).

The integrated *f*-ratio for the upper 50 m is shown in Fig. 16a. Early in the simulation the *f*-ratio is quite high (0.8) as the predominant source of nitrogen for phytoplankton nutrition is nitrate, owing to a paucity of ammonium early in the bloom. As heterotrophs accumulate and produce ammonium, the *f*-ratio drops to approximately 0.4 by day 128. Although there are no direct measurements of the *f*-ratio for the first leg, Bender *et al.* (1992) used the rate of disappearance of nitrate computed from the observations and the rate of carbon incorporation measured in the ^{14}C incubations to compute an average *f*-ratio of 0.37. However, because of the previously mentioned bias in the observations of moving from a warm feature to a colder feature, the rate of nitrate disappearance was probably underestimated, resulting in underestimation of the *f*-ratio.

A comparison of the simulated optical properties with observations is shown in Fig. 16b. During the first leg the diffuse attenuation coefficient for photosynthetically available radiation increases by roughly 70% due to the accumulation of chlorophyll in the water column. The model agrees quite well with the data.

7.2. *Late/Inside*

The evolution of the model temperature profile is shown in Fig. 17a. It agrees quite well with the data taken inside the Small eddy on days 142 through 151 (Fig. 17b). The surface temperatures for the model and data are both about 13.6°C on day 142. A fairly sharp seasonal thermocline is centered at approximately 40 m. By day 151 the surface temperature has risen about 0.2°C and the seasonal thermocline has deepened and broadened slightly.

Figure 18a shows the model evolution of the nitrate profile. In general there is good agreement with the data (Fig. 18b). On day 142 the surface values are between 1μM and 2 μM, and the nitracline is centered at 40 m. Nitrate is removed from the surface waters during the time series, and the transition to surface values below 1 μM occurs on day 143 in both the model and the data. The nitracline deepens and broadens slightly from days 142 to 151. Although the location and magnitude of the nitracline are consistent with the observations, the gradient in the model is confined to a narrower depth interval. This is primarily a result of the fact that the model mixed layer is slightly deeper than the data indicate during this time. There is also some finer scale structure in the data (perhaps spatial) that is not represented in the model.

The evolution of the model phytoplankton profile is shown in Fig. 19a. The main

Fig. 12. (a) The evolution of the phytoplankton nitrogen profile for the Early/Outside simulation. The dashed line indicates the location of the mixed layer depth during the time series. The dashed–dotted line denotes the extent of the chlorophyll data shown in (b).

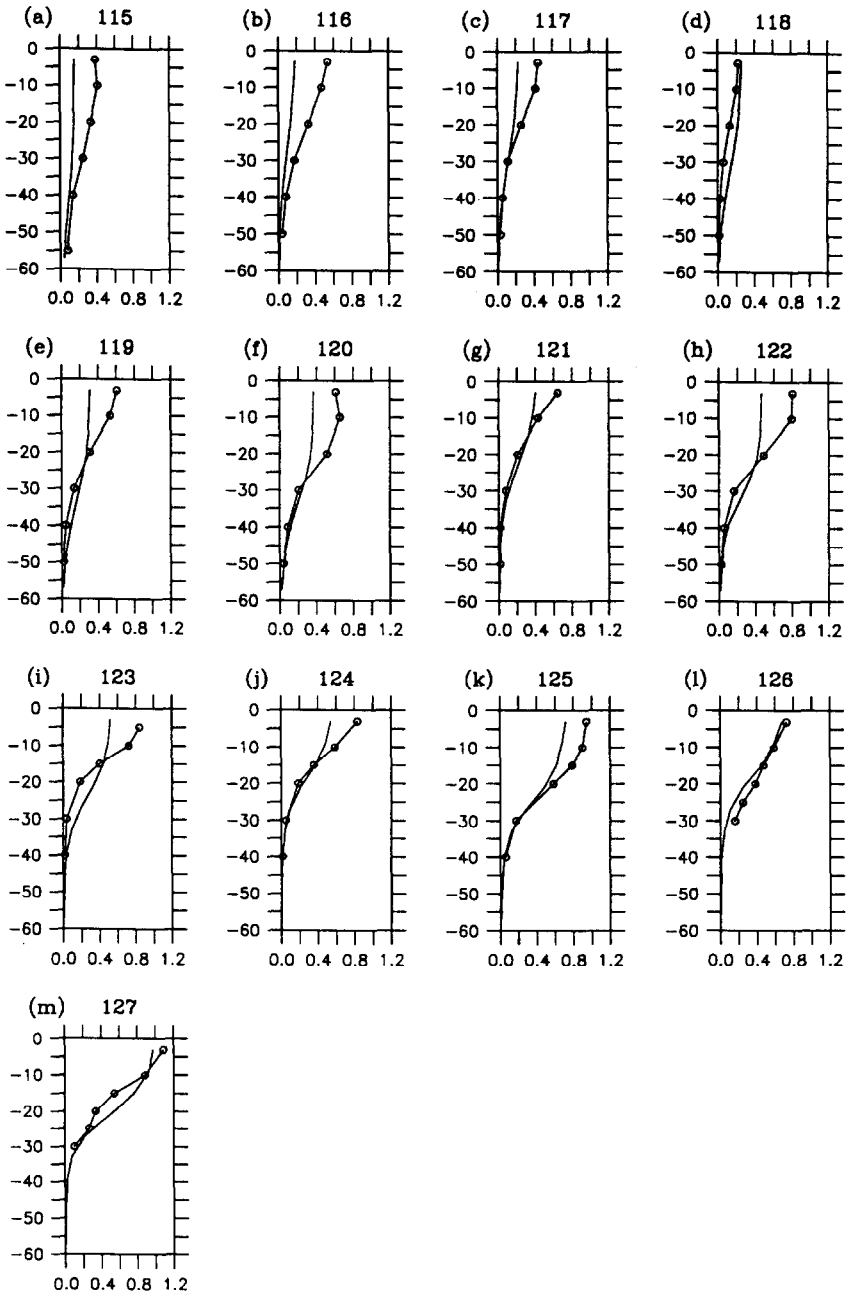

Fig. 13. Comparison of simulated primary productivity (solid lines) with ^{14}C incubations (open circles connected by solid lines) for days (a) 115, (b) 116, (c) 117, (d) 118, (e) 119, (f) 120, (g) 121, (h) 122, (i) 123, (j) 124, (k) 125, (l) 126, (m) 127.

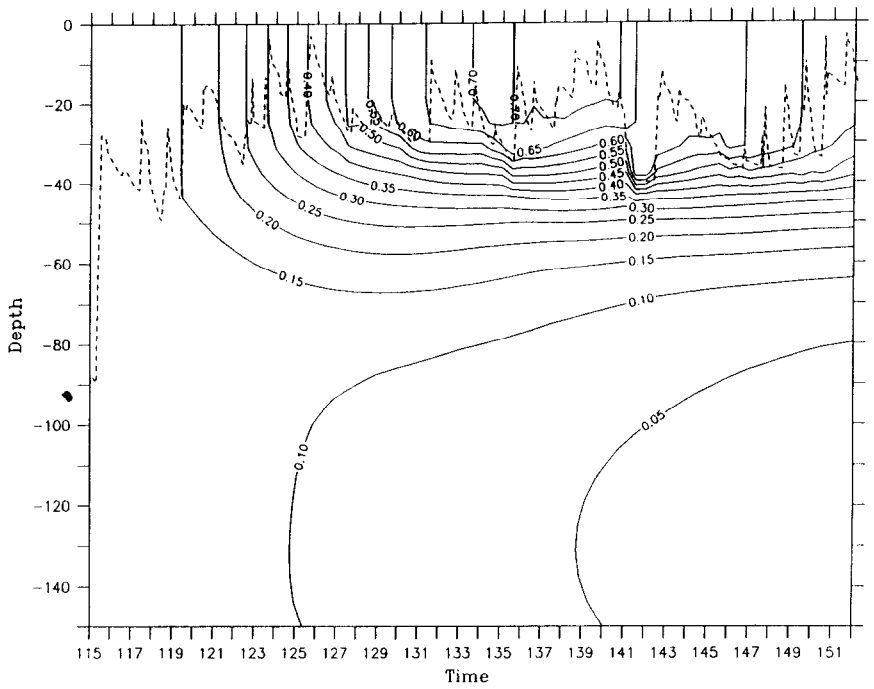

Fig. 14. The evolution of the heterotroph profile for the Early/Outside simulation. The dashed line indicates the location of the mixed layer depth during the time series.

features are in general agreement with the data (Fig. 19b). The surface phytoplankton first increases slightly and then begins to decrease. The magnitudes of the standing stocks and relative changes are not in exact agreement, but this difference is within the uncertainty in the chlorophyll to nitrogen ratio. It is interesting to note that there is more vertical structure in the chlorophyll data than there is in the model. One possible explanation for this could be photoadaptation by the cells in the real ocean that is not represented in the present model. That is, the observed subsurface chlorophyll maxima may be a result of an increase in the chlorophyll to nitrogen ratio, not an increase in phytoplankton biomass. There are many other potential explanations for the differences between the model and data, including changes in species composition, patchiness of the populations, etc. However, without more data it is impossible to assess these possibilities.

A comparison of simulated primary productivity profiles with data from *in situ* ^{14}C incubations is shown in Fig. 20. The agreement between the model and the data is quite good except for the last day (151) on which the model significantly underpredicts near surface productivity. Term by term analysis of the biological model equations facilitates diagnosis of the cause of this discrepancy. Figure 21 shows a time series of the nutrient limitation factor Q in the phytoplankton growth equation (equation 10) for this simulation. Between days 142 and 149 phytoplankton growth is only weakly constrained by nutrient availability with Q values of approximately 0.75 in the upper 20 m. After day 149 Q falls precipitously to values below 0.55, indicating the onset of significant nutrient limitation. It therefore appears that the reduced rate of primary productivity in the model was a result of a slightly premature transition to oligotrophy.

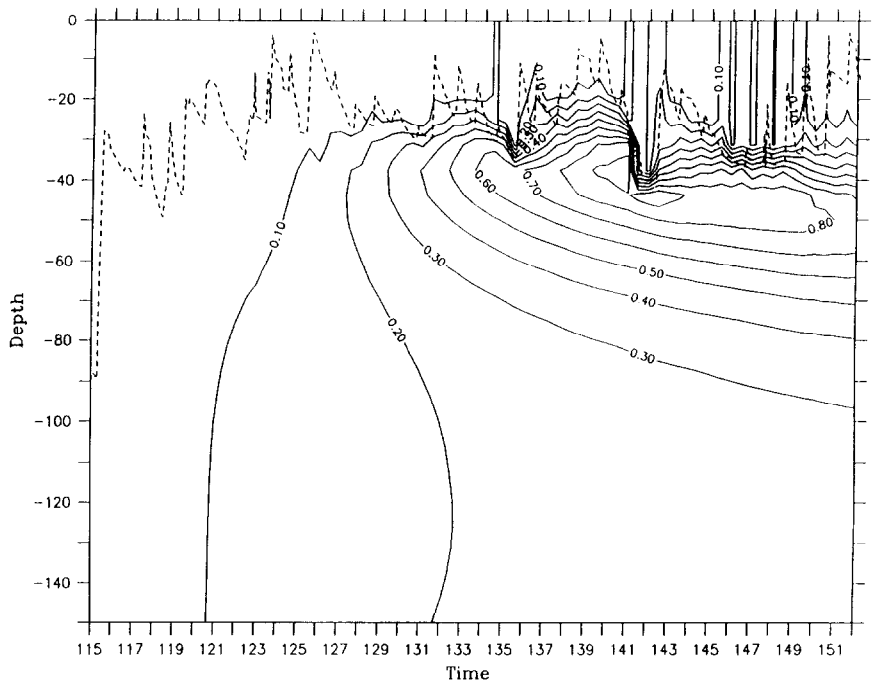

Fig. 15. The evolution of the ammonium profile for the Early/Outside simulation. The dashed line indicates the location of the mixed layer depth during the time series.

Time series of the heterotrophic population is shown in Fig. 22. Again the heterotrophic bloom is commensurate with that of the phytoplankton. Peak values of approximately 0.7 μM N occur in the mixed layer on day 135 and persist throughout the rest of the simulation. Data are available for some zooplankton size classes during this time period. Dam *et al.* (1993) documented the biomass distribution of the mesozooplankton (200–2000 μm) and found that their grazing impact on phytoplankton was quite small (only a few percent of total primary production). Sieracki *et al.* (1993) showed that the mesozooplankton represent a small (10% or less) fraction of the total heterotrophic biomass. These data are consistent with the hypothesis that the microzooplankton are the dominant grazers of phytoplankton. Sieracki *et al.* (1993) also examined the 2–20 μm size fraction of the heterotrophic nanoplankton. Although their distribution is patchy and shows some vertical structure, the integrated biomass in the upper 30 m is relatively constant between days 141 and 151 (see Sieracki *et al.*, Table 3). This pattern is consistent with the model heterotrophic distribution in that abundance in the mixed layer changes little during this time period. However, the vertical structure within the mixed layer in the heterotrophic nanoplankton data is not represented in the model as the motility of these organisms is not included in the formulation. Exact quantitative biomass comparisons are made difficult by a variety of factors, including uncertainty in the carbon to nitrogen ratio of these organisms and the fact that some size classes were poorly sampled. However, the mean microzooplankton biomass for this period reported by Sieracki *et al.* is 2100 mgC/m^2 (Table 3, total heterotrophs minus bacteria minus mesozooplankton). Converted to

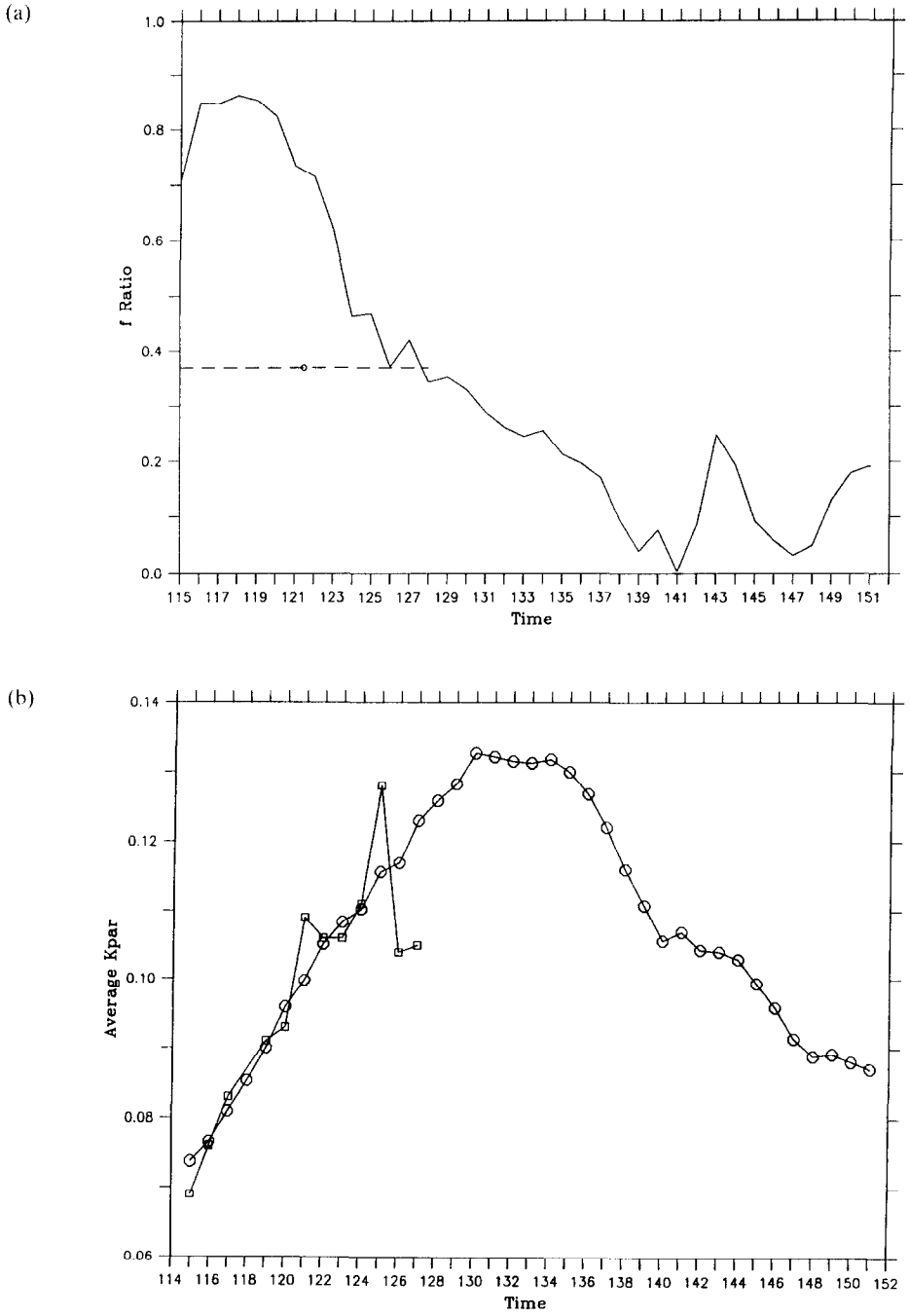

Fig. 16. (a) A time series of the depth integrated *f*-ratio for the Early/Outside simulation. The Bender *et al.* (1992) estimation of the Leg 1 *f*-ratio is denoted as an open circle with a dashed line to indicate the temporal extent of the data used to compute this average value (see text). (b) A time series of the simulated (circles) and measured (squares) diffuse attenuation coefficient for photosynthetically available radiation.

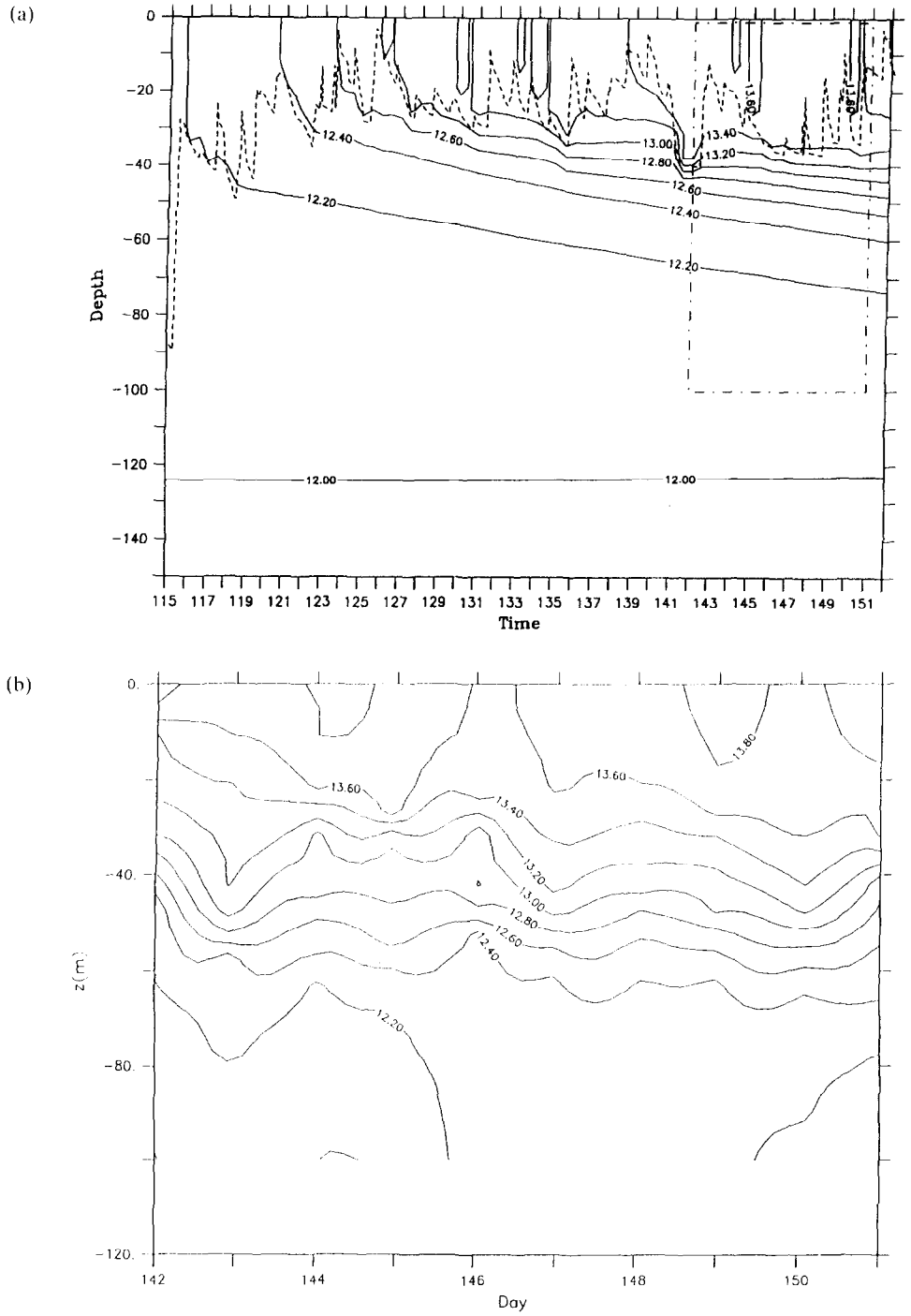

Fig. 17. (a) The evolution of the temperature profile for the Late/Inside simulation. The dashed line indicates the location of the mixed layer depth during the time series. The dashed–dotted line denotes the extent of the data shown in (b).

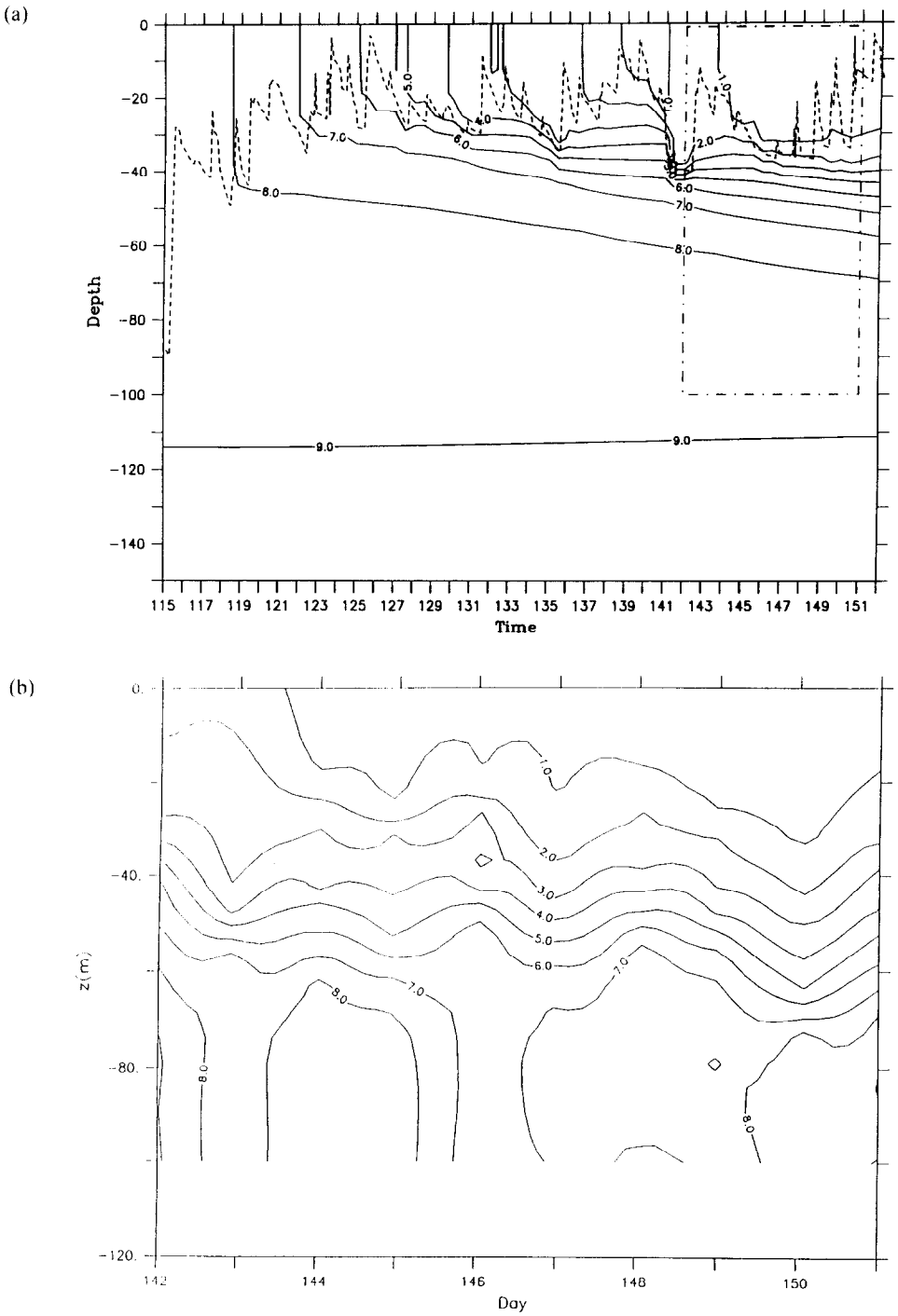

Fig. 18. (a) The evolution of the nitrate profile for the Late/Inside simulation. The dashed line indicates the location of the mixed layer depth during the times series. The dashed–dotted line denotes the extent of the data shown in (b).

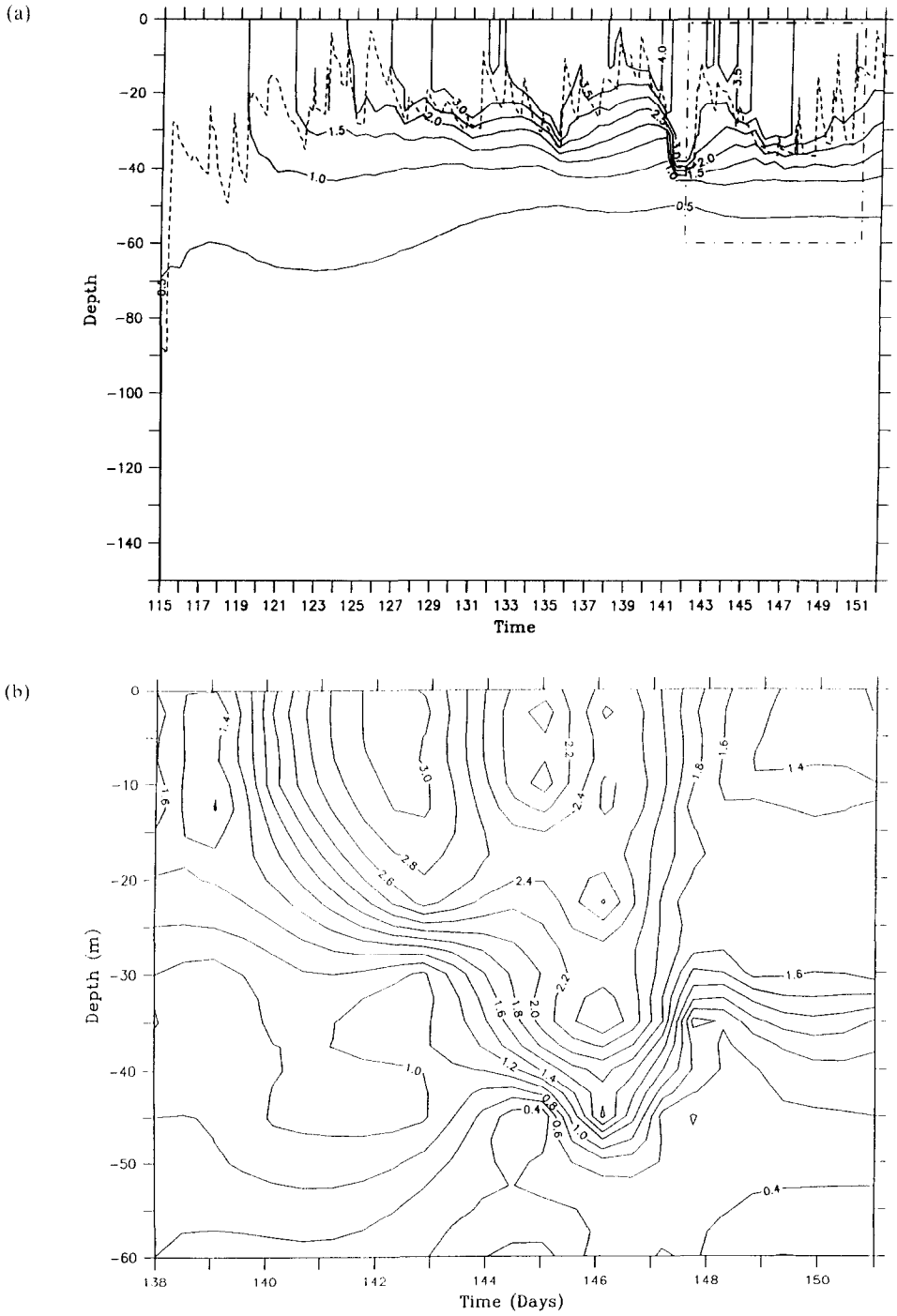

Fig. 19. (a) The evolution of the phytoplankton nitrogen profile for the Late/Inside simulation. The dashed line indicates the location of the mixed layer depth during the time series. The dashed–dotted line denotes the extent of the data shown in (b).

Table 3. Normalized root mean square sensitivity of the seven diagnostic quantities to parameter variations of magnitude δ (relative units)

Parameter		δ	NO_3				P		H			NH_4			PP			f			N_E	
1	k_w	—	—	—	—	—	—	—	—	—	—	—	—	—	—	—	—	—	—	—	—	—	—
2	k_c	0.2	1.50	1.01	1.25	4.44	3.11	3.78	1.29	0.89	1.09	0.68	0.44	0.56	2.56	3.24	2.90	0.65	0.89	0.77	0.59	0.50	0.54
3	P_{max}	0.2	2.35	5.11	3.73	7.33	12.04	9.68	1.51	5.27	3.39	1.85	3.55	2.70	6.16	8.10	7.13	1.58	1.05	1.31	1.08	2.56	1.82
4	p_1	0.2	0.64	1.31	0.97	1.82	3.77	2.79	0.47	1.02	0.75	0.45	0.75	0.60	1.89	1.90	1.90	0.43	0.50	0.46	0.30	0.50	0.40
5	p_2	—	—	—	—	—	—	—	—	—	—	—	—	—	—	—	—	—	—	—	—	—	—
6	k_1	—	—	—	—	—	—	—	—	—	—	—	—	—	—	—	—	—	—	—	—	—	—
7	k_2	—	—	—	—	—	—	—	—	—	—	—	—	—	—	—	—	—	—	—	—	—	—
8	k_n	0.2	1.00	0.65	0.82	2.87	1.78	2.33	0.72	0.48	0.60	0.78	0.68	0.73	1.20	1.89	1.54	0.34	0.49	0.42	0.35	0.28	0.32
9	R_m	0.2	5.65	1.89	3.77	16.16	15.50	15.83	6.85	2.81	4.83	4.24	0.97	2.61	8.85	7.28	8.07	2.61	2.27	2.44	2.21	2.08	2.15
10	Λ	1.0	1.55	0.53	1.04	4.24	8.21	6.22	2.20	3.78	2.99	0.87	1.81	1.34	2.64	2.33	2.48	0.96	2.56	1.76	0.73	1.49	1.11
11	γ	0.2	0.69	1.38	1.03	5.01	6.55	5.78	1.11	1.34	1.22	0.93	1.47	1.20	2.47	1.84	2.16	0.72	0.60	0.66	0.76	0.48	0.62
12	n_1	0.4	0.59	1.50	1.04	3.38	5.25	4.32	1.21	1.30	1.25	0.20	0.68	0.44	1.88	1.85	1.87	0.60	0.63	0.62	0.08	0.49	0.29
13	n_2	0.2	0.83	2.73	1.78	5.79	10.62	8.21	1.83	2.81	2.32	0.37	1.82	1.09	3.44	4.21	3.82	1.05	1.46	1.25	0.53	0.53	0.53
14	ε_1	0.2	0.14	0.16	0.15	0.73	0.63	0.68	0.13	0.10	0.11	1.08	1.07	1.07	0.38	0.37	0.38	0.26	0.25	0.25	0.68	0.69	0.69
15	ε_2	0.2	0.26	0.32	0.29	1.24	0.94	1.09	0.22	0.13	0.17	0.79	0.78	0.79	0.91	0.72	0.81	0.35	0.34	0.35	0.90	0.92	0.91
16	w_{sink}	0.2	0.13	0.12	0.13	0.59	0.55	0.57	0.05	0.05	0.05	0.07	0.08	0.07	0.26	0.33	0.29	0.08	0.09	0.09	0.02	0.01	0.01
17	f_w	0.2	0.19	0.17	0.18	0.74	0.68	0.71	0.07	0.06	0.07	0.06	0.07	0.06	0.35	0.46	0.41	0.09	0.10	0.10	0.05	0.04	0.04

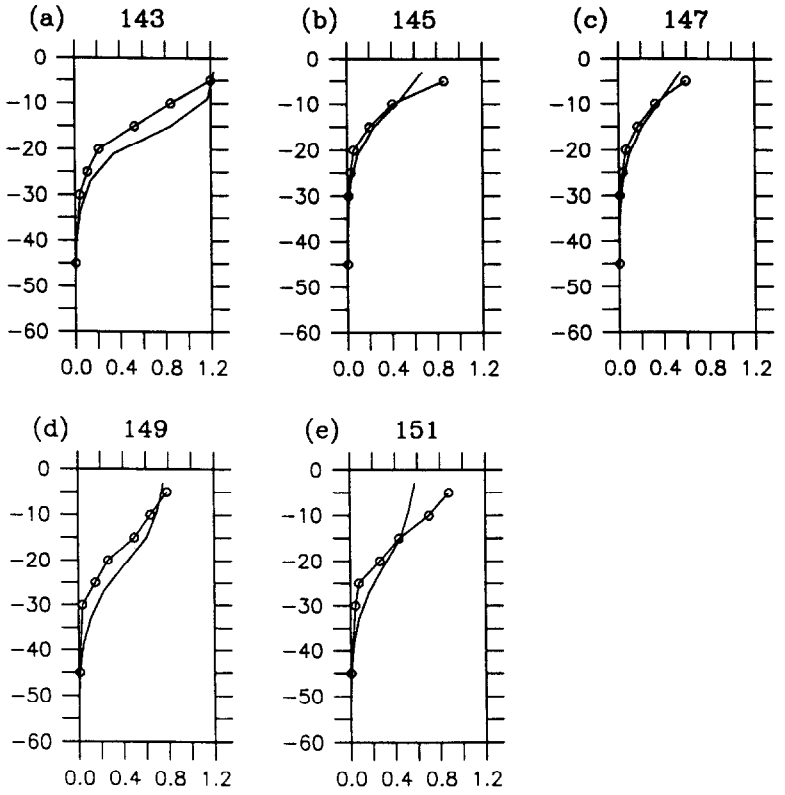

Fig. 20. Comparison of simulated primary productivity (solid lines) with ^{14}C incubations (open circles connected by solid lines) for days (a) 143, (b) 145, (c) 147, (d) 149, (e) 151.

nitrogen units according to the Redfield ratio, this corresponds to 0.87 μM N which is quite similar to the model predicted value.

The evolution of the model ammonium concentration is shown in Fig. 23a. It agrees quite well with the data shown in Fig. 23b. A subsurface maximum has developed centered at about 45–50 m with maximum values that increase with time. The data indicate an increase in the subsurface maximum from around 0.7 μM to approximately 1.4 μM, while the model increases from 1.1 μM to about 1.3 μM. Measurable quantities of ammonium are present somewhat deeper in the model than indicated by the data. The lack of ammonium at depths below about 80 m in the data may be a result of uptake by autotrophs that live deep in the water column (such as cyanobacteria) that are not represented in the model. Alternatively the excess ammonium at depth in the model may be a result of the omission of nitrification processes in the model formulation. These processes are generally thought to occur only near the bottom of the euphotic zone (Wada and Hattori, 1971; Ward, 1987; Ward & Zafiriou, 1988) yet recent evidence suggests nitrification can occur in the nitracline at depths as shallow as 6% surface light intensity (Ward *et al.*, 1989).

The simulated integrated *f*-ratio agrees reasonably well with the *f*-ratio computed from the ratio of nitrate uptake to total uptake measured experimentally (Fig. 24a). Momentarily depressed by an injection of ammonium into the mixed layer due to mixing caused by the storm on day 141, the simulated *f*-ratio is approximately correct at the start of the

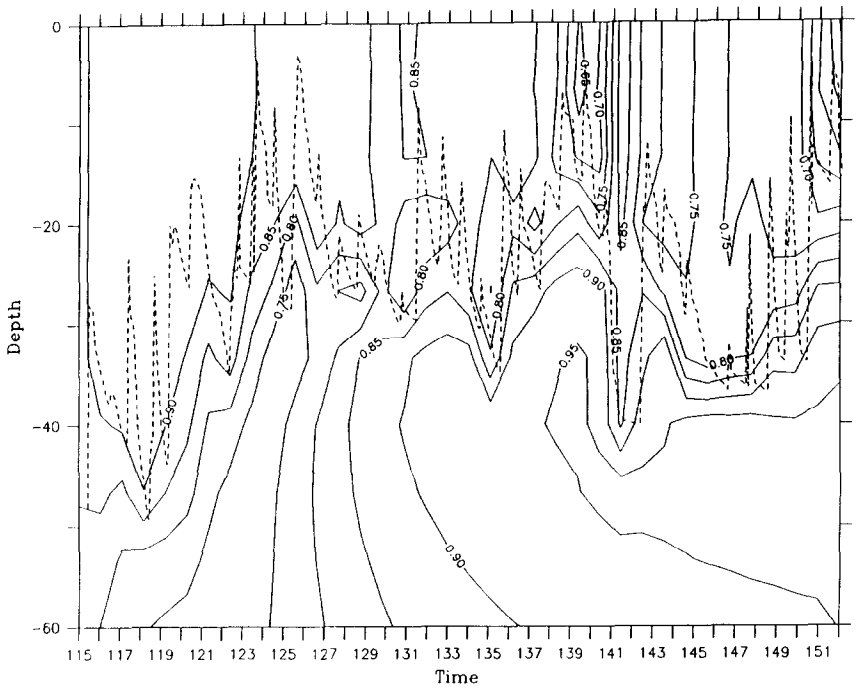

Fig. 21. The evolution of the nutrient limitation factor Q for the Late/Inside simulation.

observations on day 143. From days 146 to 148, the model f-ratio is too low, but agrees well with the data on days 149 and 151.

A comparison of the simulated optical properties with observations is shown in Fig. 24b. The model agrees well with the data that are available for the latter part of the simulation. Note that this simulation also agrees well with the observations collected outside the eddy early in the time period. This results from the fact that early in the bloom phytoplankton growth is almost entirely light limited. Because the Early/Outside and Late/Inside simulations have exactly the same initial phytoplankton biomass and similar growth rates, the phytoplankton accumulation in the early bloom of the two runs is almost identical.

7.3. *Quasi-equilibrium solutions*

The preceding simulations demonstrate the efficacy of the one dimensional model in representing the general features of the spring bloom. However, in analyzing the behavior of these solutions to the biological model equations, it is important to differentiate between the response caused by external forcing and that which is a result of the model adjusting to initial conditions which may not necessarily be at equilibrium. In order to ascertain how much of the behavior in these simulations was simply a result of adjustment to the biological initial conditions, a simulation was conducted in which the mixed layer depth was held constant at its initial depth of 90 m. The overall character of these quasi-equilibrium solutions is quite different from the simulations described above (not shown). Although there is some accumulation of phytoplankton and removal of nutrients, the

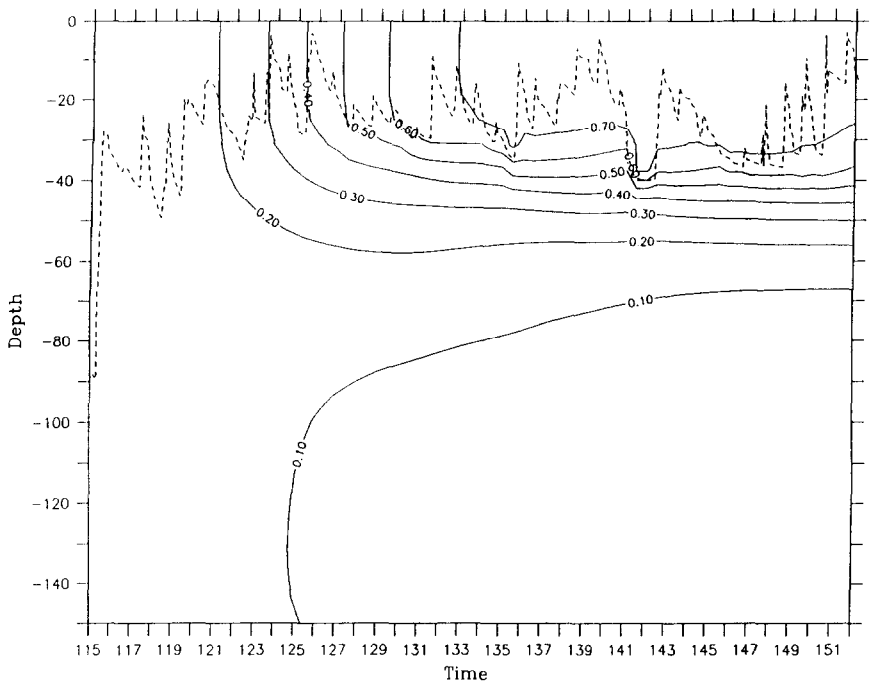

Fig. 22. The evolution of the heterotroph profile for the Late/Inside simulation. The dashed line indicates the location of the mixed layer depth during the time series.

magnitude of the bloom is greatly reduced as is the nutrient drawdown. Hence it can be concluded that the behavior of the Early/Outside and Late/Inside simulations is mostly a forced response rather than adjustment to disequilibrium in the initial conditions.

8. PARAMETER DEPENDENCE AND SENSITIVITY ANALYSIS

It is of interest to understand how the model solutions depend on the various parameters and how sensitive the solutions are to particular choices of those parameters. To accomplish this a set of numerical experiments were conducted in which the parameters were systematically varied about the central values used in the preceding section. These central values are considered to be the most realistic insofar as they produce a model trajectory that best represents the observations. Each of the experiments described below consists of two simulations, one in which a given parameter is increased and one in which it is decreased. The differences in the qualitative behavior between these simulations and the central run (inside the Small eddy) will elucidate the dependence of the solution on the

Fig. 23. (a) The evolution of the ammonium profile for the Late/Inside simulation. The dashed line indicates the location of the mixed layer depth during the time series. The dashed–dotted line denotes the extent of the data shown in (b).

(a)

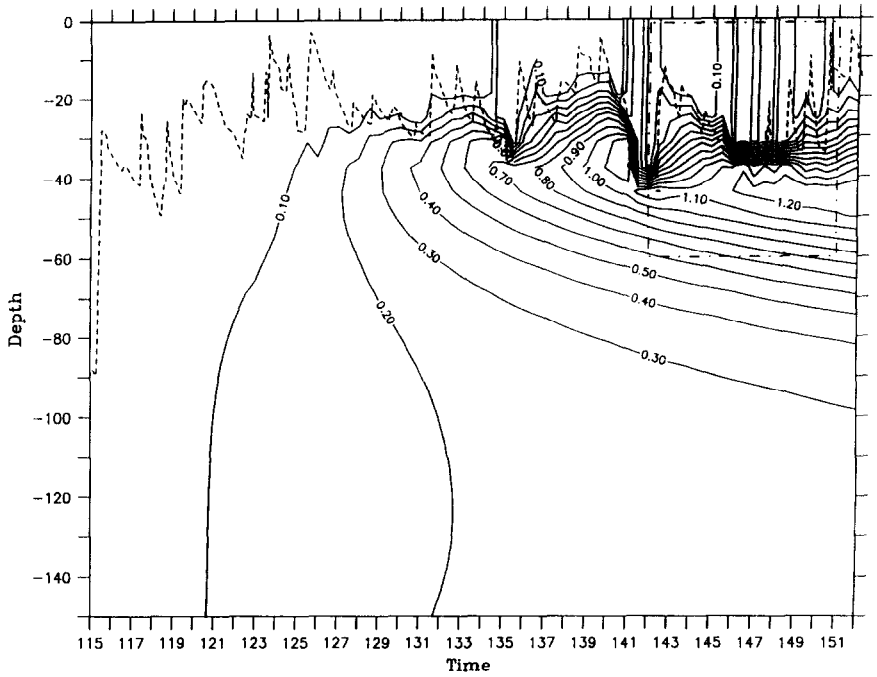
Depth
0
-20
-40
-60
-80
-100
-120
-140
115 117 119 121 123 125 127 129 131 133 135 137 139 141 143 145 147 149 151
Time

(b)

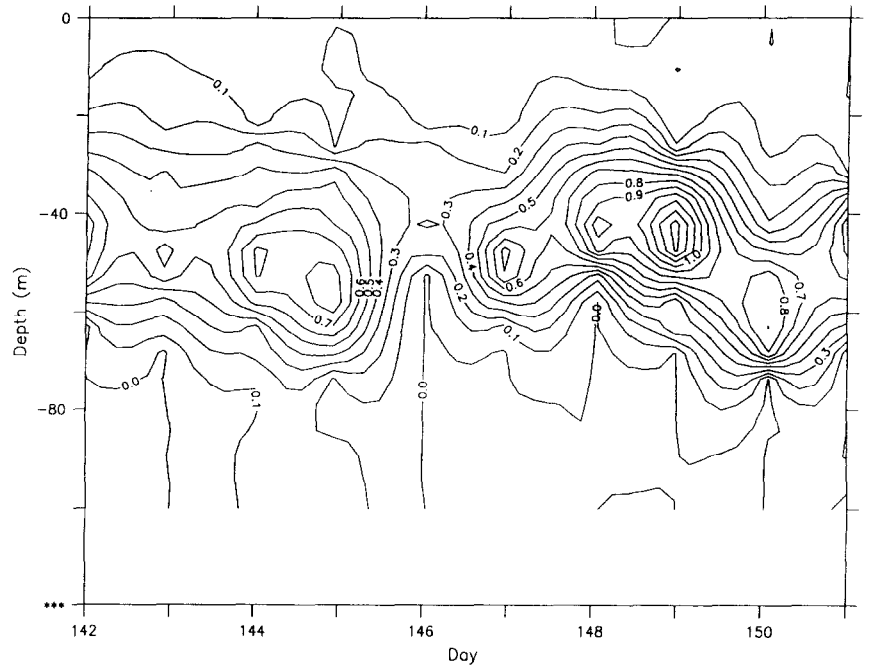
Depth (m)
0
-40
-80
142 144 146 148 150
Day

NH_4

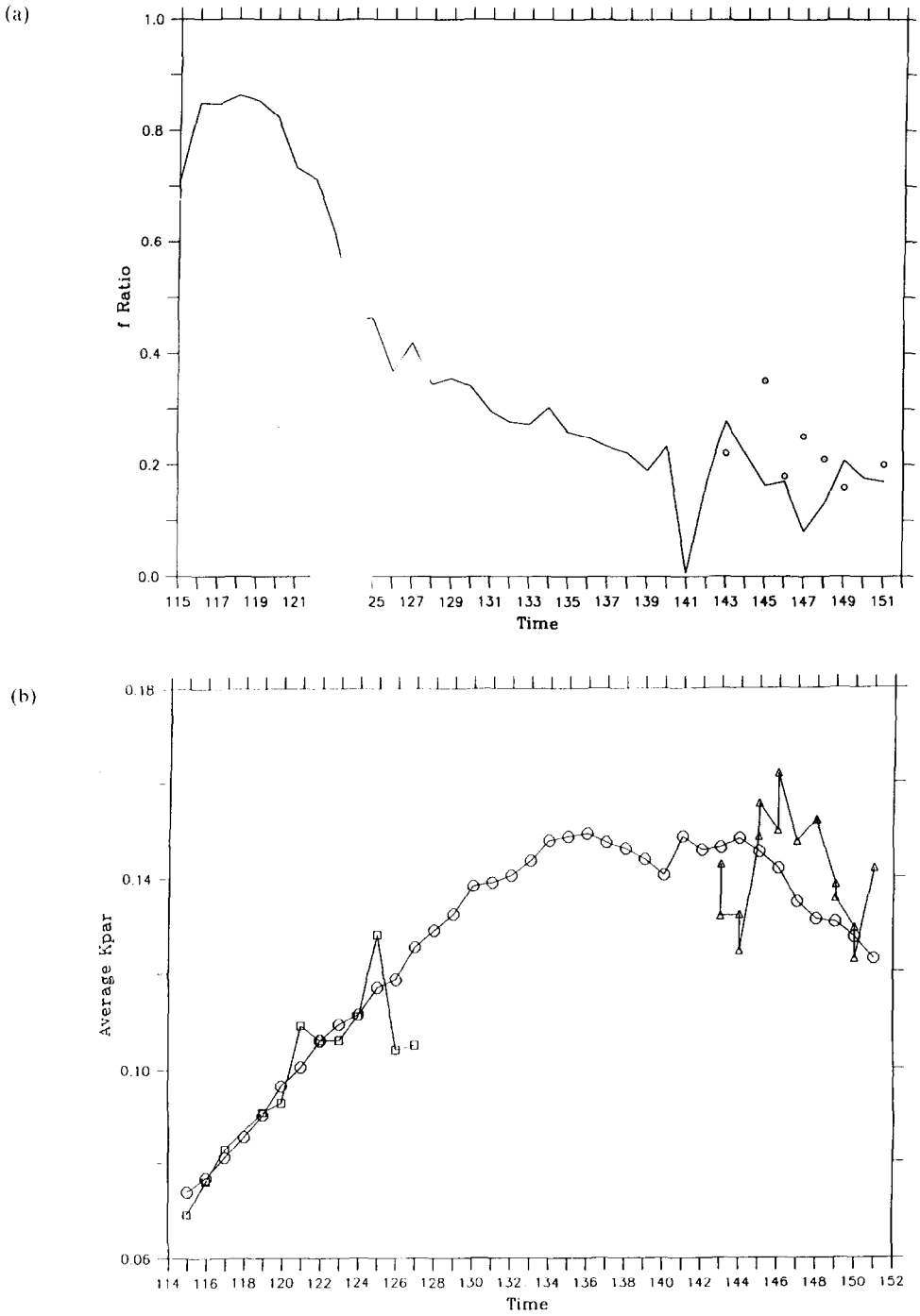

Fig. 24. (a) A time series of the integrated *f*-ratio for the Late/Inside simulation. Estimates based on data by McCarthy and Nevins (1993) are shown as open circles. (b) A time series of the simulated (circles) and measured (Leg 1: squares; Leg 2: triangles) diffuse attenuation coefficient for photosynthetically available radiation.

parameter. A quantitative estimate of normalized parameter sensitivity $S(P)$ is computed in a manner similar to Fasham *et al.* (1990):

$$S(P) = \frac{\dfrac{1}{t_2 - t_1}\displaystyle\int_{t_1}^{t_2} \frac{D(P) - D_c}{D_c}\,dt}{\left|\dfrac{P - P_c}{P_c}\right|}$$

The numerator is the temporally integrated normalized root mean square difference between a particular diagnostic quantity in a sensitivity run $D(P)$ and the value of that diagnostic for the central run D_c. This root mean square difference is normalized by the magnitude of the parameter perturbation from its value P_c in the central run. The diagnostic quantities used in this analysis are time series of spatially integrated nitrate, phytoplankton, heterotrophs, ammonium, exported nitrogen, primary production and *f*-ratio. For brevity the time series of diagnostic quantities is shown for only one parameter sensitivity experiment (P_{max}). The results of the remaining experiments will be described and presented in summary form only (see below). The normalized sensitivites of the seven diagnostic quantities to each parameter are listed in Table 3 and displayed graphically in Fig. 25. The parameters k_w, P_2, k_1 and k_2 have been excluded from this analysis because they are well constrained by data, either from the NABE or the literature.

As an example, consider the maximum rate of photosynthesis P_{max}. This parameter sets the scale of the phytoplankton growth rate expression. Of the seven diagnostic quantities, this parameter affects phytoplankton and primary productivity the most, for obvious reasons (Fig. 25b). Increasing P_{max} causes the bloom to occur earlier and much more phytoplankton nitrogen accumulates during its peak (Fig. 26). The change in the timing and magnitude of the bloom causes nitrate to be drawn down more rapidly. The integrated nitrate curve flattens out as the nitrate in the surface waters is depleted. Subsequent to the onset of oligotrophy, heterotrophs rapidly consume the excess phytoplankton nitrogen, so that after day 140 the integrated phytoplankton curve is nearly coincident with that of the central run. Nutrient recycling by the larger heterotrophic biomass causes increases in both the ammonium and exported nitrogen reservoirs, while leaving the *f*-ratio relatively unaffected.

When P_{max} is decreased, there is hardly any bloom at all. Heterotrophs overtake the phytoplankton population before and significant bloom occurs. At this growth rate, phytoplankton simply cannot outpace the heterotrophic grazing pressure. There is a marked asymmetry in the model response to this parameter perturbation, owing to the fact that the most salient feature of the simulation has dramatically changed in character. Much less nitrate is removed from the water column than in the central run. Heterotrophs accumulate early in the simulation (albeit at a slower rate) but after day 135 they cannot meet their respiratory demands and therefore begin to die out. Much less ammonium is generated in this simulation, and nitrogen export is also reduced.

The normalized sensitivity of each of the seven diagnostics to the various parameters is summarized in Fig. 27. By far the two most sensitive parameters are the maximum growth rates for phytoplankton and heterotrophs (parameters 3 and 9). Unfortunately, these are parameters for which no direct measurements are available during NABE. Because these rates are so crucial to the functioning of the ecosystem, it would be advisable to make such observations in future experiments of this type. The model solutions are also quite

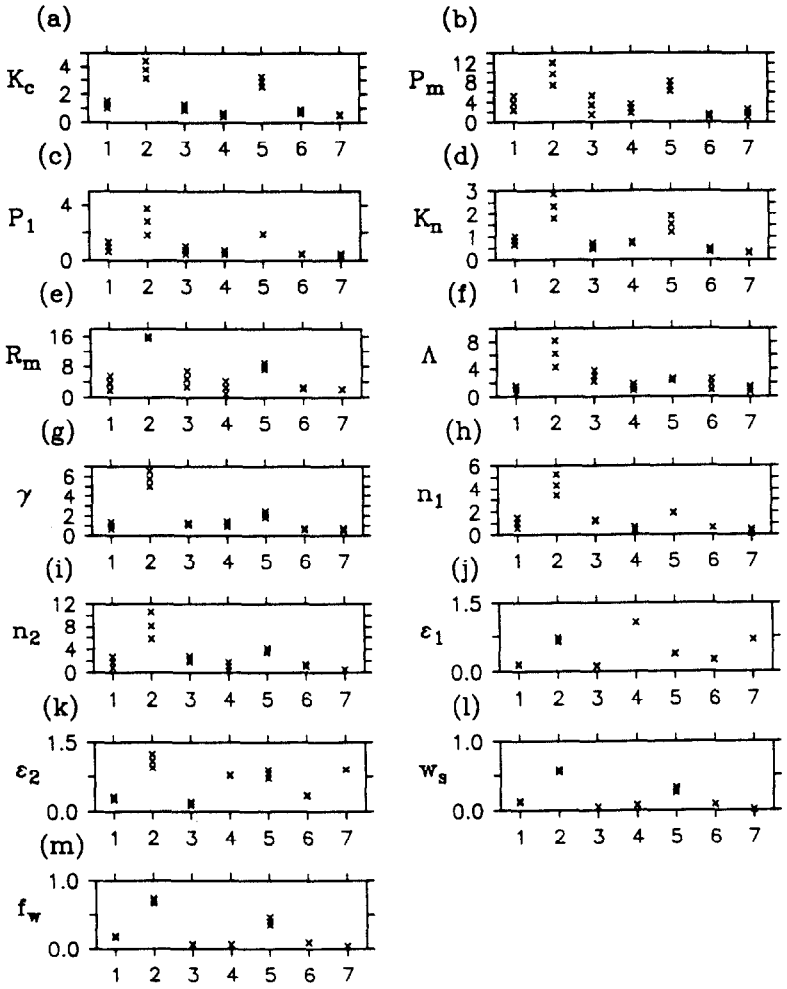

Fig. 25. Root mean square difference in the seven diagnostic quantities for the parameter sensitivity experiments. Numerals 1 through 7 correspond to (1) nitrate (2) phytoplankton (3) heterotrophs (4) ammonium (5) primary production (6) *f*-ratio (7) exported nitrogen. In each instance the values are shown for the high and low perturbations in addition to a mean value computed from the two cases.

sensitive to the quadratic heterotrophic loss rate (parameter 13), particularly as they relate to integrated nitrate, phytoplankton, heterotrophs, primary production and *f*-ratio. These sensitivities indicate that the balance between consumption and production is a critical factor in determining the character of the bloom.

9. SUMMARY AND CONCLUSIONS

A flexible three dimensional coupled physical and biological model has been introduced. It has been shown that a one dimensional implementation of this model is capable of capturing the general features of the spring bloom in the North Atlantic. However,

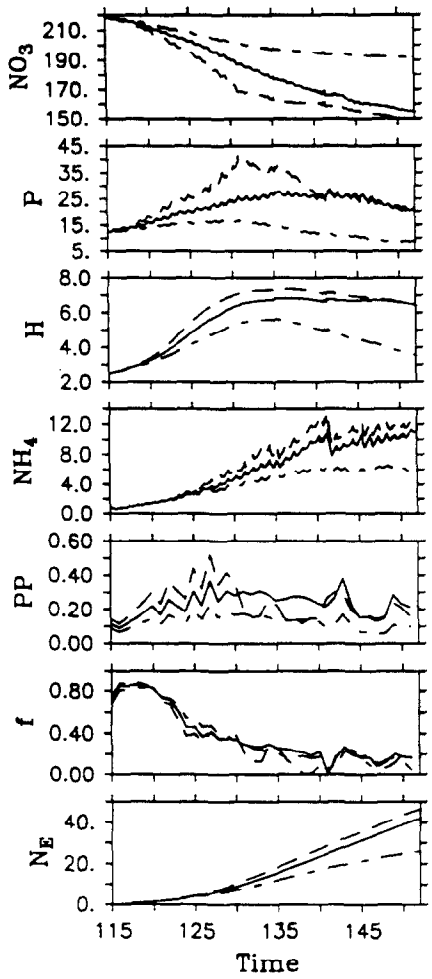

Fig. 26. Trajectories of integrated nitrate, phytoplankton, heterotrophs, ammonium, primary production, *f*-ratio and exported nitrogen for the central run (solid lines) and the simulations in which P_{max} is higher (dashed lines) and lower (dashed–dotted lines) than the optimal value.

explicit treatment of the mesoscale variability within the one dimensional framework is critical to the success of the fit. The fact that the two main observational periods sampled different mesoscale water masses at different times (one early outside the Small eddy and one later inside the eddy) poses a problem because the initial "pre-bloom" nitrate profiles are quite different due to the mesoscale perturbation of the density surfaces. An assessment of this perturbation based on hydrographic and altimetric information (Robinson *et al.*, 1993) and a coherent nitrate–density relationship (Fig. 4) permit reasonable estimation of the pre-bloom nitrate profile inside the Small eddy. This provides the initial conditions required to run parallel simulations inside and outside the eddy that both start at the same time in the pre-bloom situation.

The simulation inside the eddy shows good agreement with the Late/Inside data set. The seasonal thermocline that forms in the model from an initially well mixed layer is

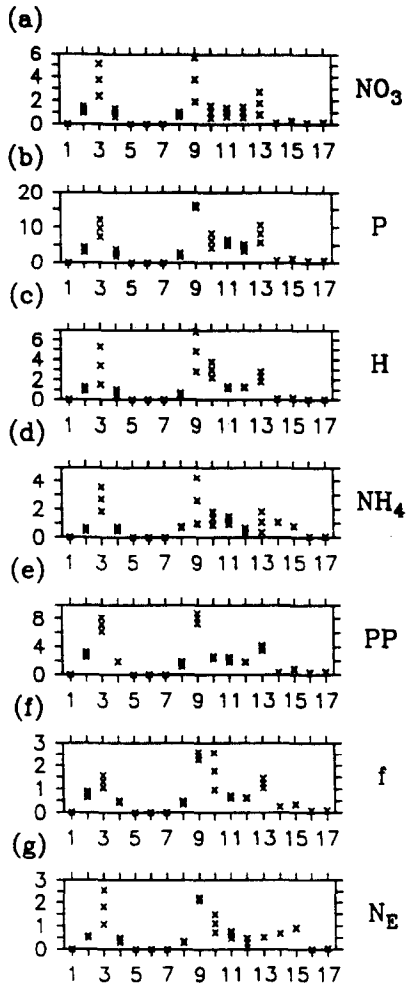

Fig. 27. Root mean square difference in the seven diagnostic quantities for the parameter variations in the sensitivity experiments. Numerals 1 through 17 correspond to the parameter numbers in Table 3. In each instance the values are shown for the high and low perturbations in addition to a mean value computed from the two cases.

consistent with the data in both strength and vertical extent. Sea surface temperatures also coincide. There is similar agreement between the model and data in the formation of the nitracline. The rate of removal during the observational period is consistent both in the mixed layer itself and in the deepening of the nitracline. Chlorophyll observations show more variability and vertical structure than model phytoplankton nitrogen during this period, but much of the discrepancy could be attributed to variations in the chlorophyll to nitrogen ratio in the phytoplankton population. Simulated primary productivity matches the data very well except for on the last day of the time series when the model began to show signs of nutrient limitation. The model forms a subsurface ammonium maximum from an initially homogeneous profile that compares well with the observations. Model generated *f*-ratio is in good agreement with independent estimates based on uptake

measurements. Finally, the simulated inherent optical properties conform with bio-optical measurements.

Comparison of the simulation outside the eddy with the early time series is not as satisfactory partially because of a bias in the observations. While the late observational period is confined to the interior of the Small eddy, the early time series is somewhat biased in that the first observations are taken from a warm feature exterior to the eddy and subsequent measurements are made in cold features (the frontal region between the warm feature and the eddy and an additional cold feature to the west of the warm feature). This movement from warm to cold features causes an apparent sink of heat in the data which results in the simulated temperature profiles heating up more quickly than observed. Conversely, the bias represents an apparent source of nitrate in the data, causing the nutrient removal to seem excessive in the model. This apparent supply of nitrate reduces the estimates of utilization used by Bender *et al.* (1992) in computing an *f*-ratio for the time series, and significantly depresses their estimated *f*-ratio (0.37). Simulated *f*-ratios average almost a factor of two higher during this period (0.64). Thus, neglecting mesoscale structures in the context of the distribution of observations can significantly bias estimates of changes in water column properties with time. Put differently, spatial variability can be mistaken for temporal variability if care is not taken to separate the two. MRM95 demonstrates that the apparent discrepancy in nitrate drawdown can be reconciled with proper treatment of the space–time variability in the full three dimensional implementation of this model.

Discrepancies in phytoplankton and primary production are not as easy to understand. Phytoplankton populations are presumably light limited in the early phase of the bloom so the bias in the measurements should have less of an effect on these variables. However, primary production is systematically underestimated in the near surface region early in the time series. Agreement with observations at the end of the period is much better, but the reason for the early differences are not known. Phytoplankton nitrogen appears to build up slightly faster than chlorophyll based estimates would suggest. The degree to which phytoplankton chlorophyll to nitrogen ratios may have changed, which cannot be determined from the data, is relevant to this issue.

The two parallel simulations and sensitivity analyses corroborate early conclusions about ecosystem functioning during the bloom. There is a tight coupling between phytoplankton production and heterotrophic consumption as evidenced by the large differences in model results caused by perturbations to the phytoplankton and heterotroph growth rate parameters. In fact, grazing by heterotrophs is a major factor in regulating the phytoplankton population even early in the bloom. Not only does the heterotrophic activity decrease the amplitude of the phytoplankton biomass maximum at the peak of the bloom, it also delays the transition to oligotrophy by providing a substantial source of regenerated nutrients.

Acknowledgements—D.J.M. and A.R.R. were supported by ONR N00014-84-C-0461, N00014-90-J-1593 and N00014-93-1-0577. D.J.M. was also supported by an Office of Naval Research Graduate Fellowship and a VCAR Postdoctoral Modeling Fellowship. J.J.M. was supported by NSF OCE88-17830. The biological and chemical data sets used in this study were provided by numerous investigators both directly and via the JGOFS database. The help of George Heimerdinger, the manager of the U.S. JGOFS Data Management office is gratefully appreciated. His meticulous superintendence and expedient distribution of the data sets contributed a great deal to this effort. The following investigators are acknowledged for their various data sets: R. T. Williams, hydrography and nutrients; C. Knudson, W. S. Chamberlin and J. Marra, primary production and diffuse

attenuation; C. O. Davis and W. J. Rhea, bio-optical chlorophyll measurements; C. Garside, nutrients; S. Fitzwater and J. Martin, primary productivity and chlorophyll; W. Broenkow, irradiance; C. Trees, diffuse attenuation. The helpful comments of four anonymous reviewers are greatly appreciated.

REFERENCES

Alldredge A. and C. C. Gotschalk (1989) Direct observations of mass flocculation of diatom blooms: characteristics, settling velocities and formation of diatom aggregates. *Deep-Sea Research*, **36**, 159–171.

Bender M., H. Ducklow, J. Kiddon, J. Marra and J. Martin (1992) The carbon balance during the 1989 spring bloom in the North Atlantic Ocean, 47N, 20W. *Deep-Sea Research*, **39**, 1707–1725.

Bienfang P. (1981) Sinking rates of heterogeneous, temperate phytoplankton populations. *Journal of Plankton Research*, **3**, 235–253.

Broenkow W., R. E. Reaves and M. A. Yarbrough (1990) JGOFS North Atlantic Bloom long track and vertical profiling results. Technical Report MLML 90-1, Moss Landing Marine Laboratory, Moss Landing, CA.

Capriulo G. (1990) *Ecology of marine protozoa*. Oxford University Press, New York.

Dam H., C. A. Miller and S. H. Jonasdottir (1993) The tropic role of mesozooplankton at 47N, 20W during the North Atlantic Bloom Experiment. *Deep-Sea Research II*, **40**, 197–212.

Ducklow H. and R. P. Harris (1993) Introduction to the JGOFS North Atlantic Bloom Experiment. *Deep-Sea Research II*, **40**, 1–8.

Fasham M., P. M. Holligan and P. R. Pugh (1983) The spatial and temporal development of the spring phytoplankton bloom in the Celtic Sea, April 1979. *Progress in Oceanography*, **12**, 87–145.

Fasham M., H. W. Ducklow and S. M. KcKelvie (1990) A nitrogen-based model of plankton dynamics in the oceanic mixed layer. *Journal of Marine Research*, **48**, 591–639.

Garside C. and J. C. Garside (1993) The "f-ratio" on 20°W during the North Atlantic Bloom Experiment. *Deep-Sea Research II*, **40**, 75–90.

Garwood R. (1977) An oceanic mixed layer model capable of simulating cyclic states. *Journal of Physical Oceanography*, **7**, 455–468.

Gill A. E. (1982) *Atmosphere–ocean dynamics*. Academic Press, New York.

Glover D. and P. G. Brewer (1988) Estimates of wintertime mixed layer nutrient concentrations in the North Atlantic. *Deep-Sea Research*, **35**, 1525–1546.

Goldman J. and P. M. Glibert (1983) Kinetics of inorganic nitrogen uptake by phytoplankton. In *Nitrogen in the marine environment*, E. Carpenter and D. G. Capone, editors, chapter 14, Academic Press, New York, pp. 487–512.

Kirk J. (1983) *Light and photosynthesis in aquatic ecosystems*. Cambridge University Press, Cambridge.

Klein P. and B. L. Hua (1988) Mesoscale heterogeneity of the wind-driven mixed layer: influence of a quasigeostrophic flow. *Journal of Marine Research*, **46**, 495–525.

Knudson C., W. S. Chamberlain and J. Marra (1989) Primary production and irradiance data for the U.S. JGOFS (leg 2) *Atlantis II* (Cruise 112.4). Technical Report LDGO-89.4, Lamont-Doherty Geological Observatory, Palisades, NY.

Lorenzen C. (1972) The extinction of light in the ocean by phytoplankton. *J. Cons. Int. Explor. Mer.* **34**, 262–267.

Marra J. and C. Ho (1993) Initiation of the spring bloom in the northeast Atlantic (47N, 20W): a numerical simulation. *Deep-Sea Research II*, **40**, 55–74.

Martin J., S. E. Fitzwater, R. M. Gordon, C. N. Hunter and S. J. Tanner (1993) Iron, primary production and carbon–nitrogen flux studies during the JGOFS North Atlantic Bloom Experiment. *Deep-Sea Research II*, **40**, 115–134.

McCarthy J. (1981) The kinetics of nutrient utilization. In *The physiological bases of phytoplankton ecology*, T. Platt, editor, pp. 211–233. *Canadian Bulletin of Fish and Aquatic Science*.

McCarthy J. and J. L. Nevins (1986) Utilization of nitrogen and phosphorous by primary producers in warm core ring 82-B following deep convective mixing. *Deep-Sea Research*, **33**, 1773–1788.

McGillicuddy D. (1993) *Mesoscale ocean dynamics and biological productivity*. PhD thesis, Harvard University, Cambridge, MA 02138.

McGillicuddy D., A. R. Robinson and J. J. McCarthy (1995) Coupled physical and biological modeling of the spring bloom in the North Atlantic (II): three dimensional bloom and post-bloom effects. *Deep-Sea Research*, this issue.

Mullin M. M., E. F. Stewart and F. J. Fuglister (1975) Ingestion by planktonic grazers as a function of concentration of food. *Limmology and Oceanography*, **20**, 259–262.

Parsons T., M. Takahashi and B. Hargrave (1984) *Biological oceanographic processes*. Pergammon Press, New York.

Platt T., C. L. Gallegos and W. G. Harrison (1980) Photoinhibition of photosynthesis in natural assemblages of marine phytoplankton. *Journal of Marine Research*, **38**, 687–701.

Press W., B. P. Flannery, S. A. Teukolsky and W. T. Vetterling (1986) *Numerical recipes*. Cambridge University Press, Cambridge.

Rhea W. and C. O. Davis (1990) Bio-Optical Profile Data Report: Joint Global Ocean Flux Study North Atlantic Bloom Experiment R.V. *Atlantis II* Leg 2 (25 April–10 May 1989). Technical report, Jet Propulsion Laboratory, Pasadena, CA.

Riley G. (1942) The relationship of vertical turbulence and spring diatom flowerings. *Journal of Marine Research*, **5**, 67–87.

Robinson A. (1993) *Physical processes, field estimation and interdisciplinary ocean modeling*. Reports in Meteorology and Oceanography. Harvard University, Cambridge, MA.

Robinson A., D. J. McGillicuddy, J. Calman, H. W. Ducklow, M. J. R. Fasham, F. E. Hoge, W. G. Leslie, J. J. McCarthy, S. Podewski, D. L. Porter, G. Saure and J. A. Yoder (1993) Mesoscale and upper ocean variabilities during the 1989 JGOFS bloom study. *Deep-Sea Research II*, **40**, 9–35.

Slagle R. and G. Heimerdinger (1991) U.S. Joint Global Ocean Flux Study North Atlantic Bloom Experiment Data Report, April–July 1989. WHOI/JGOFS Process Study Data Report P-1.

Steele J. (1974) Spatial heterogeneity and population stability. *Nature*, **248**, 83.

Steele J. and E. W. Henderson (1981) A simple plankton model. *The American Naturalist*, **117**, 676–691.

Steele J. and M. M. Mullin (1977) Zooplankton dynamics. In *The sea*, E. Goldberg, editor, John Wiley and Sons, New York, pp. 857–890.

Stevenson J. (1983) The seasonal variation of the surface mixed layer response to the vertical motions of linear Rossby waves. *Journal of Physical Oceanography*, **13**, 1255–1268.

Sverdrup H. (1953) On conditions for the vernal blooming of phytoplankton. *J. Cons. Explor. Mer.* **18**, 287–295.

Syrett P. (1981) Nitrogen metabolism of microalgae. In *The physiological bases of phytoplankton ecology*, T. Platt, editor, pp. 182–210. *Canadian Bulletin of Fish and Aquatic Science*.

Wada E. and A. Hittori (1971) Nitrate metabolism on the euphotic layer of the central North Pacific Ocean. *Limnology and Oceanography*, **16**, 766–772.

Walstad L. and A. R. Robinson (1993) A coupled Surface Boundary Layer–Quasigeostrophic Model. *Dynamics of Atmospheres and Oceans*, **18**, 151–207.

Ward B. (1987) Nitrogen transformations in the Southern California Bight. *Deep-Sea Research*, **34**, 785–805.

Ward B. and O. C. Zafiriou (1988) Nitrification and nitric oxide in the oxygen minimum of the eastern tropical North Pacific. *Deep-Sea Research*, **35**, 1127–1142.

Ward B., K. A. Kilpatrick, E. H. Renger and R. W. Eppley (1989) Biological nitrogen cycling in the nitracline. *Limnology and Oceanography*, **34**, 493–513.

Wheeler P. and S. A. Kokkinakis (1990) Ammonium recycling limits nitrate use in the oceanic subarctic Pacific. *Limnology and Oceanography*, **35**, 1267–1278.

Woods J. (1988) Mesoscale upwelling and primary production. In *Toward a theory on biological–physical interactions in the world ocean*, B. Rothschild, editor, D. Reidel, Dordrecht.

Wroblewski J. (1977) A model of phytoplankton plume formation during variable Oregon upwelling. *Journal of Marine Research*, **35**, 357–394.